



Out-of-plane seismic retrofitting of masonry walls with Textile Reinforced Mortar composites

Stefano De Santis¹ · Gerardo De Canio² · Gianmarco de Felice¹ · Pietro Meriggi¹ · Ivan Roselli²

Received: 21 January 2019 / Accepted: 7 August 2019 / Published online: 9 September 2019
© Springer Nature B.V. 2019

Abstract

Masonry walls are particularly vulnerable against out-of-plane seismic actions. Steel tie-bars and crowing beams in reinforced masonry can prevent their overturning, but collapse may take place also by bending, leaf separation or disaggregation. Textile Reinforced Mortar (TRM) composites, comprising high strength fabrics and inorganic matrices, can be applied to effectively improve the seismic capacity of masonry load-bearing walls and infill panels. Nevertheless, a deeper knowledge on the dynamic response and ultimate capacity of retrofitted walls still needs to be gained before TRM systems can be confidently used in engineering practice. This work describes a shake table test carried out on two full-scale wall specimens, one made of regular tuff blocks and one of two leaves of rubble stones, subjected to seismic out-of-plane vertical bending. The walls were tested unreinforced, repaired and strengthened with TRMs and tested again. A unidirectional textile of ultra high tensile strength steel was used on the tuff wall, whereas a bidirectional basalt mesh was applied over the entire surface of the stone wall, with the addition of transversal steel connectors. The responses of the specimens before and after retrofitting are compared to show the improvement of acceleration and displacement capacity entailed by TRM retrofitting and the modification of deflection profiles, failure modes, damage development and dynamic properties. Test outcomes prove the effectiveness of TRM composites for the protection of existing masonry structures, including architectural heritage, in earthquake prone areas and provide information on the reliability of analytical predictions for seismic assessment.

Keywords Basalt Textile Reinforced Mortar · Fabric Reinforced Cementitious Matrix · Out-of-plane bending · Shake table · Steel Reinforced Grout · 3DVision

✉ Stefano De Santis
stefano.desantis@uniroma3.it

¹ Department of Engineering, Roma Tre University, Rome, Italy

² Department for Sustainability (SSPT-MET-DISPREV), ENEA Casaccia Research Centre, Rome, Italy

1 Introduction

Collapses surveyed after recent earthquakes demonstrate that masonry walls are particularly vulnerable against out-of-plane seismic actions (see, amongst others: D'Ayala and Paganoni 2011; Dizhur et al. 2016; Sorrentino et al. 2018). In old historic structures, which do not exhibit a box-type behaviour, perimeter walls often collapse by overturning, as a result of the limited tensile strength of the material and of the weak connection with orthogonal walls and horizontal structures (Lourenço et al. 2011). Traditional retrofitting devices, such as steel tie-bars and crowning beams in reinforced masonry, proved effective in preventing, or at least delaying, the onset of overturning mechanisms. Nevertheless, collapse may still occur under either vertical or horizontal bending, both in load-bearing unreinforced masonry walls and in infill panels belonging to reinforced concrete frame structures. Finally, leaf separation or disaggregation may take place, especially in historic structures, whose walls exhibit weakly connected leaves (often with an inner core of rubble stones or pebbles), high percentages of voids, weak mortar and irregular arrangement (Giarretton et al. 2017). The type and shape of the failure mechanism and the level of seismic intensity that activates it depend upon the mechanical properties of masonry, the wall section morphology and layout of masonry (size and shape of the units, thickness and regularity of the joints), the interaction with other structural members (return walls, floors, roof) and the presence of openings (Costa et al. 2012; de Felice et al. 2017).

Given the importance of protecting the health and life of people in earthquake prone areas and of minimizing the risks associated with earthquake induced damage on the building stock, a number of studies have been carried out to tackle the challenging issue of the out-of-plane seismic behaviour of masonry walls (Sorrentino et al. 2017). Nonetheless, a deep understanding of the seismic response of existing masonry structures and on the most appropriate retrofitting technologies still needs to be gained. To this end, Textile Reinforced Mortar (TRM) composites, comprising high strength textiles externally bonded to the structural members by inorganic matrices, can be efficiently used for structural retrofitting. In addition to TRM, other names and acronyms are used in the literature, including Fabric Reinforced Cementitious Matrix (FRCM), Fabric Reinforced Mortar (FRM) and, when comprising steel textiles, Steel Reinforced Grout (SRG). All these systems share the same technology, which can be seen as an evolution either of Fibre Reinforced Polymers (FRP) (Hamed and Rabinovitch 2010; Velazquez-Dimas et al. 2000), in which the organic matrix is replaced by an inorganic one, or of *ferrocement* (Chen 2010; Gattesco and Boem 2015), in which the steel mesh is substituted by fabrics with higher strength and durability performances, allowing for thinner overlays (Papanicolaou et al. 2008).

TRM composites offer versatility, easy and fast installation and high mechanical performances with negligible mass increase, thanks to their elevated strength-to-weight ratio. Furthermore, they can be integrated in the plaster layer during the ordinary maintenance works of the façades, as a compatible, sustainable and cost-efficient solution (Papanicolaou et al. 2008). Finally, they are particularly suitable for, even if they are not limited to, the seismic protection of architectural heritage, because, when a lime-based mortar matrix is used, they comply with the criteria of conservation, such as physical/chemical compatibility with historic substrates, vapour permeability and reversibility.

Extensive research has been carried out in the last decade on the tensile and bond behaviour of TRM composites (e.g., de Felice et al. 2014; Carozzi et al. 2014; D'Antino et al. 2014; Razavizadeh et al. 2014; De Santis 2017; Dalalbashi et al. 2018), as well as on their use for strengthening reinforced concrete (Babaeidarabad et al. 2014a, b; Colajanni et al.

2014; Napoli and Realfonzo 2015; Gonzalez-Libreros et al. 2017) and masonry (Papanicolaou et al. 2008, 2011; Garmendia et al. 2014; Fossetti and Minafò 2015; Alecci et al. 2016; Marcari et al. 2017; De Santis et al. 2018b, 2019) structures. These studies provided important information on the mechanical behaviour of TRMs and of retrofitted structural members and led to the development of testing (De Santis et al. 2017a; de Felice et al. 2018), acceptance (Ascione et al. 2015; De Santis et al. 2018a) and design (ACI 2013; CNR 2018) recommendation documents. On the other hand, a deeper knowledge needs to be developed on the seismic response of structures reinforced with TRM systems and on the gain in seismic capacity that can be achieved.

2 Background and significance

Despite the development of TRM composites is still at a relatively early stage, the promising perspective of using them for the strengthening of existing masonry structures, has already fostered a number of experimental studies. Many of them were devoted to the flexural behaviour, which can be significantly enhanced thanks to the tensile strength provided by the fabric. Medium scale wall panels have been tested under three/four point bending (see, amongst others, Papanicolaou et al. 2008, 2011; Valluzzi et al. 2014; Kariou et al. 2018) placed horizontally and subjected to vertical loads, monotonically or cyclically increased to failure. On the one hand, the efforts required by bending tests in terms of setup preparation and test execution are relatively limited, making it possible to repeat the tests with varying configurations. On the other hand, the lack of axial compression poses the problems that no reliable tests on reference unreinforced specimens are available for comparison and that the loading conditions differ from those experienced in the field. To overcome these shortcomings, experimental investigations have been performed on full-scale specimens placed vertically and subjected to out-of-plane concentrated forces (Bellini et al. 2017; Gattesco and Boem 2017), airbag pressure (Babaedarabad et al. 2014a, b), or seismic action (De Santis et al. 2016a). Experimental tests have shown the effectiveness of TRM systems for enhancing the out-of-plane flexural strength of unreinforced masonry walls and have provided important information for the development design relationships (ACI 2013; D'Antino et al. 2018; Meriggi et al. 2019). Nonetheless, as said before, a deeper knowledge still needs to be gained on the seismic behaviour of masonry structures retrofitted with TRMs before they can be confidently used in engineering practice, especially for the seismic retrofitting of architectural heritage.

To this aim, the lessons learned in the shake table tests performed to investigate the out-of-plane bending response of unreinforced masonry structures (e.g., Graziotti et al. 2016; Giaretton et al. 2017; Vaculik and Griffith 2018) indicate that it is of the utmost importance that both the boundary conditions and loads accurately represent the actual ones. As for the former ones (boundary conditions), the top horizontal displacement needs to be restrained, which clearly is needed to prevent overturning and induce bending. But it has been observed (Tondelli et al. 2016) that the response is controlled by the vertical restraint at the top. More specifically, if vertical displacements are restrained, the arching behaviour increases the flexural strength and reduces deflections, so this is a key issue in the design of the experimental setup. As for the latter ones (loads), the wall specimens should be subjected to constant axial load and dynamic (earthquake) motion at the base and on top. The distribution of the inertial forces induced by earthquakes, as well as the effects of their fast variation/inversion, are impossible to replicate with static procedures (Costa et al. 2012),

which may be overconservative in terms of estimated strength and damage (Lourenço et al. 2013), because quasi-static cycles tend to be more severe than earthquake base motion (Vaculik and Griffith 2018). Finally, given the sensitivity of the response of unreinforced masonry to compressive stresses (Derakhshan et al. 2013), the vertical component of seismic inputs should be applied in addition to the dead load.

Due to the high efforts required by shake table tests, it is impossible to test many samples and experimental outcomes are therefore insufficient, by themselves, to develop design relationships. Furthermore, they generally consist of a sequence of tests, in which seismic inputs are progressively scaled up to follow the development of damage. It is commonly accepted that the results are affected by the test sequence because damage accumulates and a method does not exist to identify a single earthquake that corresponds to the entire input sequence (de Felice et al. 2017). On the other hand, shake table tests offer the unique advantage that the dynamic nature of the loading conditions experienced by a structure during an earthquake is well represented, including the combined effect of static and seismic loads and of both horizontal and vertical components of the acceleration (provided that the shake table system is multi-axial). For this reason, shake table tests on full-scale specimens can provide fundamental information, unavailable otherwise, for the investigation of the seismic behaviour of structural members or subassemblages, for the assessment of the effectiveness of retrofitting solutions and for the validation of numerical models in dynamic loading regimes.

This work describes a shake table test carried out on two full-scale wall specimens, one made of regular tuff blocks and the other one of two leaves of rubble stones. The walls were built on a unique reinforced concrete foundation beam, which made it possible to test them together on the shake table. On top of each specimen, a reinforced brickwork top beam was built, whose horizontal displacement was constrained by a steel structure, in order to induce out-of-plane vertical bending under the earthquake base motion applied by the shake table. At the same time, its vertical displacement and rotation were left free, to replicate the constrain condition which are actually experienced by a masonry wall belonging to a building. For the same reason, an additional vertical load was applied by means of steel plates, to simulate the effect of a roof. Five natural accelerograms were applied in both horizontal and vertical directions, with increasing scale factor to collapse. The walls were tested unreinforced, then repaired and strengthened with TRM composites on both sides, and tested again. Different retrofitting solutions were designed based on the arrangement of the units (shape of the blocks and number of leaves) and on the damage pattern observed after the tests on the unreinforced specimens. More specifically, the tuff wall was retrofitted with Steel Reinforced Grout (SRG) strips, which comprised a unidirectional Ultra High Tensile Strength Steel (UHTSS) textile bonded onto the surface of the masonry with a lime-based mortar matrix. On the stone wall, instead, a Basalt Textile Reinforced Mortar (BTRM) system was used, which comprised a bidirectional basalt mesh applied over the entire surface of the specimen, to prevent disaggregation, with the same mortar used for SRG. In this case, transversal steel connectors were also installed to prevent leaf separation. Both the retrofitting solutions tested in this study are suitable for real structural applications. The seismic behaviour of the specimens was recorded by accelerometers and by a high-resolution 3D motion capture system, which makes use of wireless retro-reflecting spherical markers whose position was detected by near infrared digital cameras. The responses of the specimens before and after retrofitting are compared in terms of acceleration and displacement capacity, failure modes, damage development and dynamic properties, which were determined with different Experimental Modal Analysis approaches.

The present work aims at contributing to the advancement of the current state-of-knowledge by providing experimental evidence developed in shake table tests on full-scale specimens, with specific reference to the following issues (which, at present stage, are still open):

1. the seismic response of masonry walls under out-of-plane vertical bending induced by earthquake base acceleration and the role played by the masonry type (material and arrangement of the units);
2. the improvement of the seismic capacity, in terms of both maximum acceleration and displacement, that can be achieved by retrofitting the walls using TRM composites, designed according to the type of the masonry substrate and to the earthquake induced damage expected or developed in absence of reinforcement;
3. the modification produced by the retrofitting work in terms of dynamic properties (fundamental frequency) and deformed shape;
4. the reliability of the ultimate flexural strength estimated by design/assessment methods developed for engineering practice purposes, with the further goal of fostering the knowledge transfer from scientific research to engineering practice and the proper use of TRM composites for the protection of existing masonry structures, including architectural heritage, in earthquake prone areas.

3 Experimental setup and input signals

3.1 Wall specimens and test rig

Two full-scale wall specimens were tested on the shake table. One wall was in regular tuff masonry and one was in rubble stone masonry, and both were built using a commercial ready-mix M5 class (according to EN 998-2:2016) hydraulic lime mortar. Each specimen had 3.48 m height, 1.53 m width and 0.25 m thickness (Figs. 1, 2). The walls were built on a single reinforced concrete foundation with 0.35 m × 0.35 m cross section, which was used to move the specimens in the laboratory hall and to anchor them to the shake table, making it possible to test them together under the same input signal. The first layer of masonry was partially laid in the foundation to prevent cracking at the masonry-to-concrete interface.

The tuff wall was built with 250 mm × 370 mm × 110 mm blocks (in one leaf) and had 12.3 kN/m³ weight density (γ), 5.9 N/mm² compressive strength (f_c) and 1575 N/mm² Young's modulus (E_c). The stone wall was built with roughly squared lime stone units having 300 mm × 250 mm × 100 mm approximate average size and arranged in two leaves, partially connected by transversal stones (10/m²). It had $\gamma = 24.2$ kN/m³, $f_c = 14.3$ N/mm² and $E_c = 4522$ N/mm². With the aim of reproducing the typical characteristics of a stone masonry wall, the units were intentionally provided with an irregular arrangement, the joints had variable thickness and, locally, the mortar was missing in the joints.

On top of each wall, a 1530 mm × 270 mm × 250 mm reinforced brickwork top beam ($\gamma = 18$ kN/m³) was built with four layers of clay bricks and an M15 class (according to EN 998-2:2016) lime-based mortar. The top beams were reinforced with a steel textile (the same used for the SRG reinforcement, see §4.2.1), installed in the bed joints during construction, which provided tensile and bending strength. Each top beam was connected to the underlying masonry wall with three 600 mm long steel connectors, 0.5 m spaced, inserted in drilled holes and then injected with a lime-based grout. In order to avoid



Fig. 1 Perspectival (a) and lateral (b) views of the experimental setup for shake table tests, with details of the anchoring system to the shake table (c) and of the retaining hinged steel frames (d)

overturning and induce out-of-plane vertical bending under seismic base motion, the horizontal displacement of the top beams were constrained. Their upward displacement and their rotation, instead, were free, in order to reproduce the constrain conditions experienced by a perimeter wall at the last storey of a masonry building. It has to be noted that this is an approximation since the seismic action at the base and at the top are not expected to be identical due to the dynamic amplification over the height (Tondelli et al. 2016). To apply such constrain condition, two steel frames were placed on the shake table near the masonry walls and connected to each other on top by two IPE200 I girders (Fig. 1b). The in-plane stiffness of the frames and the bending stiffness of the girders were sufficiently high to limit the relative displacement between the bottom and the top of the wall specimens. Eight rubber hollow cylinders, having 160 mm external diameter and 20 mm thickness, were fixed to the I girders and put in contrast with the top beams, two on the front side and two on the

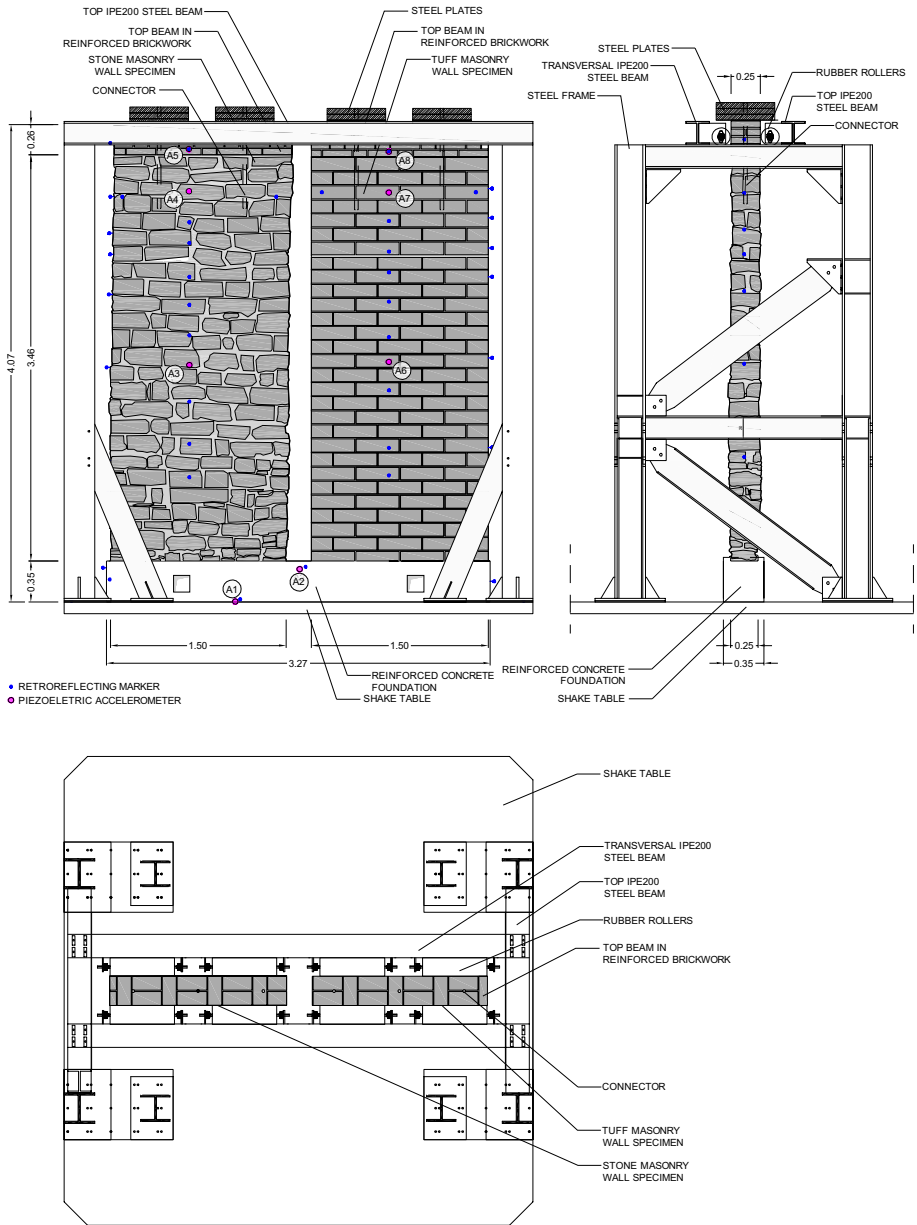


Fig. 2 Instrumentation for shake table tests

back side, for each specimen. An additional load of 6 kN was placed on top of each wall (using steel plates) to simulate the presence of a roof (e.g., a timber roof of 2 kN/m², spanning 4 m). To anchor the specimen, doubled UPN100 steel beams were placed across the foundation and were connected to the shake table by means of Ø20 mm threaded steel rods; additionally, four steel heels, two on the front and two on the back sides provided further

horizontal restraint against sliding (Fig. 1c). Finally, a retaining steel frame was placed in front of each side of each wall (in total, 4 frames), to protect the shake table and the instrumentation. The frames were hinged at the base, which made it possible to close them and block the first specimen that collapsed, allowing the tests to be continued on the other specimen (Fig. 1d).

3.2 Instrumentation

Tests were carried out on a 4 m × 4 m shake table with six degrees of freedom, ± 3 g acceleration capacity and ± 125 mm displacement capacity, controlled by four horizontal and four vertical hydraulic actuators. Piezoelectric accelerometers with $< 2\%$ accuracy and 0.01 g resolution were used to record accelerations (Fig. 2). A tri-axial accelerometer (A1) was placed on the shake table. A bi-axial one (A2) was fixed to the reinforced concrete foundation (to measure the horizontal acceleration in the out-of-plane direction and the vertical acceleration). Three uniaxial accelerometers were installed on each wall specimen (A3, A4 and A5 on the stone wall, A6, A7 and A8 on the tuff wall), to record the horizontal out-of-plane acceleration at $z = 1.70$ m, $z = 3.18$ m and $z = 3.45$ m, z being the height from the foundation; the latter one was on the top beam. Test data were acquired at 100 Hz sampling frequency and filtered using a third-order baseline correction and a fourth order Butterworth band-pass filter in the 0.35–25 Hz range, to remove errors associated with sampling and background noise introduced by the shake table system.

A high-resolution 3D motion capture system, named 3DVision (De Canio et al. 2016), was used to measure displacements. A total of 53 wireless retro-reflecting spherical markers were glued on the walls, to record their response in several points, on the top beams, to measure their deflection and verify the effectiveness of the restraint, on the foundation, to measure the seismic input actually applied to the base of the walls, and on the shake table, for reference (Fig. 2). Nine near infrared digital cameras were placed around the shake table to record the spatial displacements of the markers at 200 Hz sampling frequency. 3DVision data were post-processed with a Savitzky-Golay smoothing filter, reaching an accuracy of less than 0.1 mm (Mongelli et al. 2018). Thanks to the large number of markers monitored with 3DVision, detailed information were derived on the dynamic response of the specimens, which were used for the construction of deflection profiles and for Multi-Input/Multi-Output (MIMO) experimental modal analyses. The system offers the additional advantage that it is not affected by the range and encumbrance limitations typical of the traditional displacement sensors and it does not require the building of any stiff frame as a reference for the measurement of out-of-plane displacements. Finally, thanks to the use of cheap passive wireless markers, no relevant instrumentation damage is risked during collapse.

A 3DVision marker was glued over each accelerometer and the results provided by the two systems were compared (either by double integration of acceleration time histories or by double derivation of displacement time histories) to validate test results and calibrate filtering parameters. The instruments were placed in the same positions in the two test sessions (before and after retrofitting) to allow comparisons.

3.3 Input signals

Five input signals were selected from the European Strong Motion Database (ESD) amongst the most severe recent earthquakes in Italy: 1980 Irpinia, 1997 Umbria-Marche,

2009 L'Aquila, 2012 Emilia, 2016 Amatrice. Table 1 includes, for each of them, the date and the moment magnitude (M_w) of the event, the name and label of the record station (BGI, MRN, AMT, NCR, AQV), and the peak ground acceleration (PGA), velocity (PGV) and displacement (PGD) in horizontal and vertical directions. For the horizontal direction, the orientation (North–South or East–West) selected for the tests is specified. The scale factor of AMT record was corrected in ESD after the shake table tests were performed and the new amplitude is twice as that used in this study. The inputs are listed in the chronological order used in the tests, which was based on the horizontal PGA to obtain a sequence with increasing intensity.

The signals were applied in both the out-of-plane horizontal direction and in the vertical direction, with increasing scale factor (SF) up to the attainment of a severe damage, close to collapse. The entire test sequence performed on the unreinforced specimens was repeated from the beginning after the walls underwent repair and retrofitting with TRM composites.

The pseudo-acceleration response spectra of the input accelerograms are shown in Fig. 3, together with those of the accelerations recorded on the foundation during the tests performed with SF = 1.0 on the retrofitted specimens. The comparison proves the effective control of the shake table system, the amplitude of the recorded spectra being lower than the target ones only at high periods (above 1.5 s), which have minor structural interest. A less precise matching is also seen for the vertical components of MRN and AQV signals (Fig. 3d, j), as the shake table was not able to reach the highest peaks. Finally, tests under PGA = 0.05 g white noise (applied both horizontally and vertically), labelled as WN hereinafter, were carried out before the beginning of the tests, after each input sequence with the same SF and at the end, and were used for dynamic identification analyses.

4 Seismic behaviour of the tuff wall

4.1 Response of the unreinforced specimen

In total, 31 seismic tests were carried out on the unreinforced tuff wall, with SF ranging from 0.25 to 1.25. The specimen exhibited a nearly elastic behaviour for low intensity inputs. The mortar in the bed joint at $z = 2.60$ m crushed during test T15 (AQV, SF = 0.50, $a_{h,max} = 0.31$ g) and, from this moment on, the joint behaved as a hinge. Another hinge also progressively developed in the first bed joint above the foundation, such that the response of the wall was similar to that of a two-block system, the three hinges being the crack at the base, the crack in the middle and the top constrain provided by the rollers. The maximum acceleration of the entire test session was $a_{h,max} = 0.86$ g, recorded at T30 (AQV), the last test of the session with SF = 1.25. In the last test (T31), in which AQV input with SF = 1.25 was repeated, a further hinge developed at $z = 3.09$ m, which may be due to the activation of a second mode in the dynamic response of the wall. In test T31, the maximum displacement $\delta_{max} = 112.8$ mm of the test series was attained. It was assumed that the wall was close to collapse and, with the aim of repairing and retrofitting it, the first session of tests was concluded. The final survey revealed that, despite the mortar joints of the two hinges were crushed, the tuff blocks were not badly cracked.

The horizontal base acceleration versus out-of-plane displacement response curves ($a_h - \delta$) are plotted in Fig. 4. Since the five records used as inputs have different spectra, duration and vertical component, the response to each of them is plotted separately. Each test is

Table 1 Accelerograms selected to perform the shake table tests

| Earthquake information | | | Horizontal component | | | | Vertical component | | | |
|------------------------|---------------------------|----------------|----------------------|-----|---------|------------|--------------------|---------|------------|----------|
| # | Event | M _w | Record station | Or. | PGA (g) | PGV (mm/s) | PGD (mm) | PGA (g) | PGV (mm/s) | PGD (mm) |
| 1 | 23/11/1980, Irpinia | 6.9 | Bagnoli, BGI | E-W | 0.181 | 344 | 117.4 | 0.101 | 154 | 73.7 |
| 2 | 20/05/2012, Emilia | 6.1 | Mirandola, MRN | N-S | 0.267 | 463 | 10.3 | 0.303 | 59 | 18.7 |
| 3 | 24/08/2016, Amatrice | 6.0 | Amatrice, AMT | N-S | 0.376 | 415 | 85.4 | 0.399 | 337 | 88.7 |
| 4 | 26/09/1997, Umbria-Marche | 6.0 | Nocera Umbra, NCR | N-S | 0.492 | 326 | 26.0 | 0.398 | 212 | 27.4 |
| 5 | 06/04/2009, L'Aquila | 6.1 | L'Aquila, AQV | E-W | 0.644 | 402 | 67.8 | 0.486 | 124 | 24.5 |

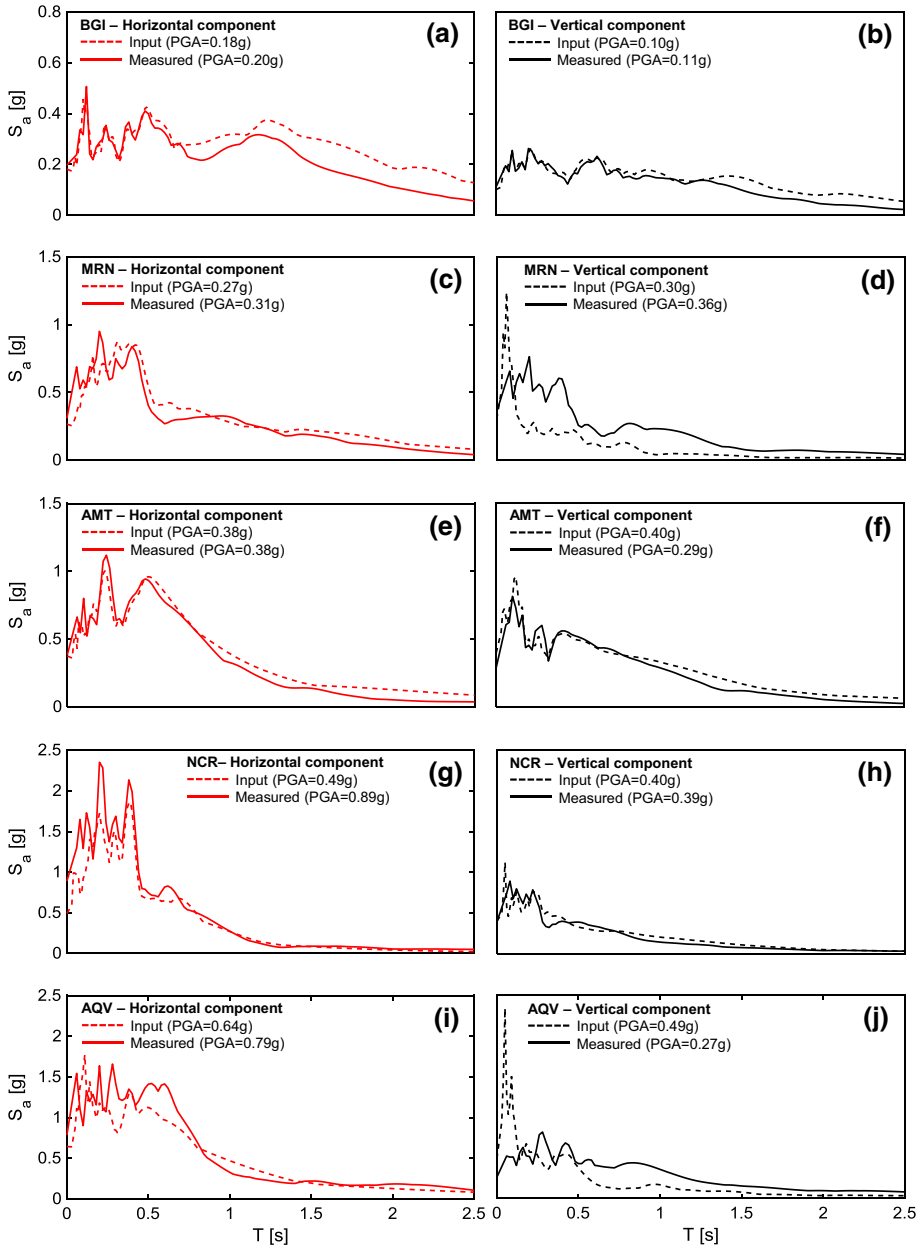


Fig. 3 Pseudo-acceleration response spectra of the signals imposed to the shake table and of those recorded on the reinforced concrete foundation during the tests with SF=1 on the reinforced specimens. Note that PGA denotes the maximum absolute acceleration

represented by two dots, associated with the maximum ($a_{h,max}$) and the minimum ($a_{h,min}$) accelerations and the corresponding (same time instant) displacements (δ_{max} and δ_{min}) measured by a marker at $z = 2.46$ m, which was the closest one to the hinge.

With the aim of deriving information on the inertial forces distributed over the wall, another response parameter, which was named as distributed acceleration (a_{distr}), was calculated as follows. The horizontal out-of-plane accelerations recorded by accelerometers 2 (foundation), 6, 7 and 8 (top beam) were taken in the time instants of $a_{h,\text{max}}$ and $a_{h,\text{min}}$. It was assumed that the acceleration varied linearly between two adjacent accelerometers (i.e., between A2 and A6, A6 and A7, and A7 and A8), so as to obtain a segmental profile over the height of the wall. The distributed acceleration was then computed as the integral of such profile divided by the total height. The resulting maximum and minimum values ($a_{\text{distr,max}}$ and $a_{\text{distr,min}}$) were in most cases higher than $a_{h,\text{max}}$ and $a_{h,\text{min}}$, due to dynamic amplification, but the shape of the $a_{\text{distr}}-\delta$ response curves is generally similar to that exhibited by the $a_h-\delta$ ones (Fig. 4).

Table 2 collects test results. More specifically, the following data are listed: the progressive test number (letter T for seismic tests and WN for tests under white noise), the signal, the scale factor (SF), the maximum and minimum base accelerations in horizontal and vertical directions ($a_{h,\text{max}}$, $a_{h,\text{min}}$, $a_{v,\text{max}}$, $a_{v,\text{min}}$), the maximum and minimum distributed accelerations ($a_{\text{distr,max}}$, $a_{\text{distr,min}}$), the displacements δ_{max} and δ_{min} and, finally, the fundamental frequency evaluated with a Single-Input/Single-Output approach (f_{SISO}) and with a Multi-Input/Multi-Output approach (f_{MIMO}).

It is worth noting that the tests performed under (nominally) identical inputs provided different results (see the two test sessions under $\text{SF}=0.50$, from T06 to T15, and the last two runs under AQV with $\text{SF}=1.25$, T30 and T31). This is due to the fact that damage progressively accumulates, so the specimen may change from test to test. Moreover, there is an unavoidable variability both of the seismic input actually replicated by the shake table and transferred to the structure through the foundation (given the same target record) as well as of the dynamic behaviour of masonry.

4.2 Strengthening with Steel Reinforced Grout

4.2.1 Reinforcement materials and layout

After the first test series, the tuff wall was repaired and reinforced with SRG (Fig. 5). Two 150 mm wide strips were bonded onto each side of the wall at 750 mm spacing (600 mm clear distance), as shown in Fig. 5b. SRG comprised a unidirectional textile of Ultra High Tensile Strength Steel (UHTSS) cords, thermo-welded on a glass mesh at 6.35 mm spacing (each 150 mm wide strip comprised 24 cords). Each cord is made of five wires, which are galvanized (coated with zinc) to provide protection against rusting, and has a cross sectional area of 0.538 mm^2 . The roughness of the cords and their spacing provide good interlocking within the mortar matrix (De Santis 2017). The textile has surface mass density $\gamma_f=670 \text{ g/m}^2$, design thickness $t_f=0.084 \text{ mm}$, tensile strength $f_t=3191 \text{ N/mm}^2$, Young's modulus $E_f=186 \text{ kN/mm}^2$ and ultimate strain $\varepsilon_f=2.19\%$ (mean values, De Santis et al. 2017b). It is worth mentioning that, even if some studies have shown that the zinc coating effectively delays corrosion under accelerated artificial aging (De Santis et al. 2016b), the long term durability of steel textiles subject to mortar carbonation and prolonged environmental exposure is still an open issue. Shear bond tests on tuff substrate provided an average bond strength (axial stress in the textile at detachment) of $f_b=1676 \text{ N/mm}^2$. The textile was bonded along the entire height of the wall, including the top beam, with a lime-based mortar having compressive strength $f_{\text{mc}}=14.5 \text{ N/mm}^2$, Young's modulus $E_m=9.6 \text{ kN/mm}^2$ and tensile strength $f_{\text{mt}}=4.6 \text{ N/mm}^2$. The tests on the unreinforced specimen suggested

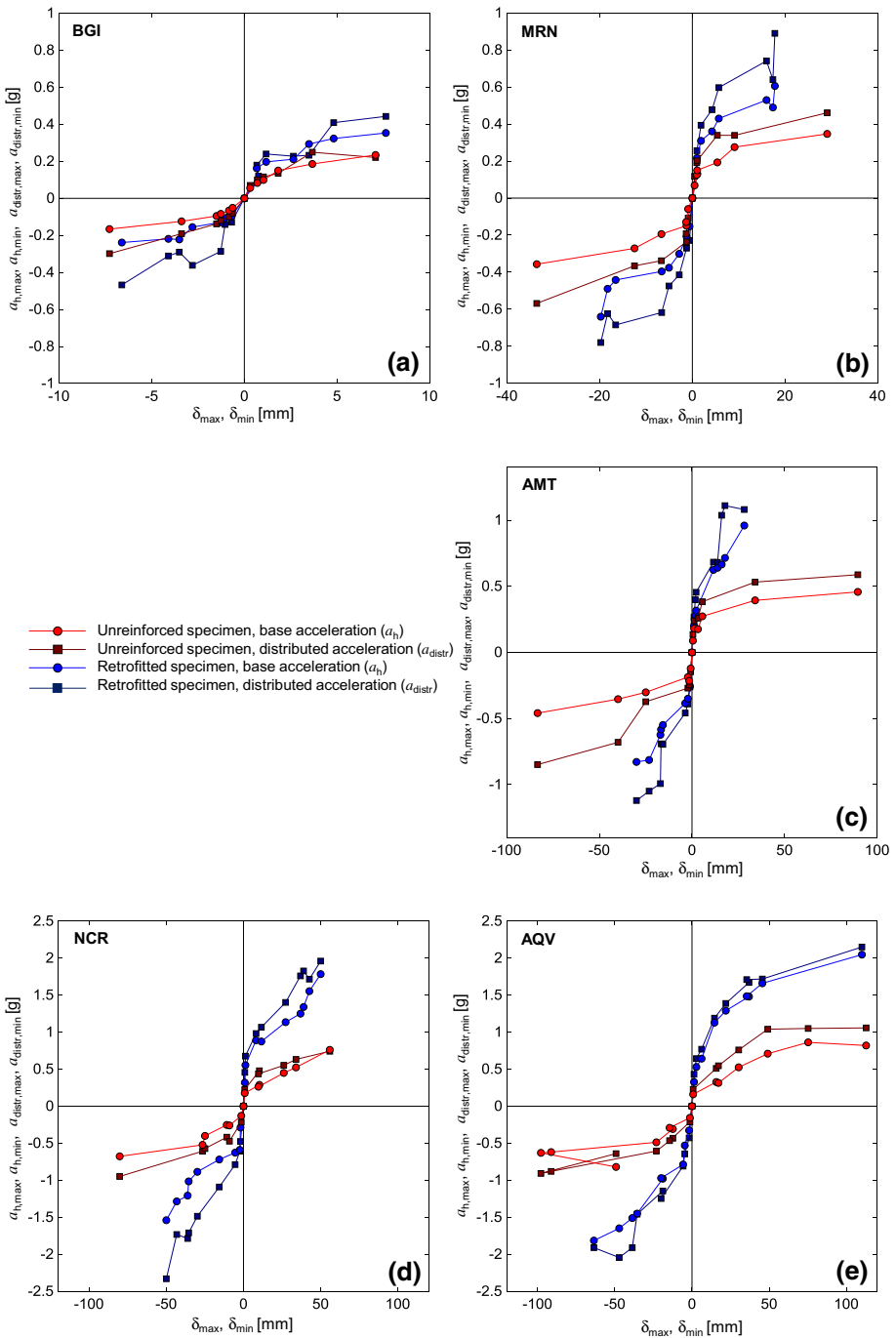


Fig. 4 Base and distributed acceleration versus displacement curves of the tuff specimen before and after SRG retrofitting under BGI (a), MRN (b), AMT (c), NCR (d) and AQV (e) seismic inputs

Table 2 Results of the tests on the unreinforced tuff wall

| Test | Signal | SF | $a_{h,max}$ | $a_{h,min}$ | $a_{v,max}$ | $a_{v,min}$ | $a_{distr,max}$ | $a_{distr,min}$ | δ_{max}^d | δ_{min}^d | f_{SISO} | f_{MIMO} |
|------------------|--------|------|-------------|-------------|-------------|-------------|-----------------|-----------------|------------------|------------------|------------|------------|
| | | – | g | g | g | g | g | g | mm | mm | Hz | Hz |
| WN01 | WN | – | | | | | | | | | 8.1 | 8.2 |
| T01 | BGI | 0.25 | 0.06 | –0.05 | 0.05 | –0.04 | 0.07 | –0.08 | 0.3 | –0.6 | 7.3 | 7.2 |
| T02 | MRN | 0.25 | 0.07 | –0.06 | 0.08 | –0.08 | 0.12 | –0.11 | 0.5 | –0.9 | 7.2 | 6.4 |
| T03 | AMT | 0.25 | 0.09 | –0.12 | 0.07 | –0.09 | 0.14 | –0.15 | 0.5 | –0.7 | 7.6 | 6.6 |
| T04 | NCR | 0.25 | 0.18 | –0.13 | 0.10 | –0.10 | 0.22 | –0.22 | 0.8 | –1.4 | 8.0 | 6.3 |
| T05 | AQV | 0.25 | 0.16 | –0.16 | 0.10 | –0.11 | 0.23 | –0.21 | 0.8 | –1.3 | 6.3 | 6.3 |
| WN 02 | WN | – | | | | | | | | | 7.0 | 6.4 |
| T06 | BGI | 0.50 | 0.08 | –0.07 | 0.06 | –0.06 | 0.10 | –0.10 | 0.7 | –0.8 | 6.6 | 6.1 |
| T07 | MRN | 0.50 | 0.13 | –0.13 | 0.12 | –0.16 | 0.19 | –0.19 | 1.0 | –1.3 | 6.2 | 5.4 |
| T08 | AMT | 0.50 | 0.18 | –0.22 | 0.13 | –0.16 | 0.24 | –0.25 | 1.1 | –1.5 | 6.0 | 5.2 |
| T09 | NCR | 0.50 | 0.29 | –0.26 | 0.15 | –0.24 | 0.48 | –0.47 | 10.3 | –9.1 | 5.6 | 4.1 |
| T10 | AQV | 0.50 | 0.33 | –0.29 | 0.13 | –0.23 | 0.51 | –0.47 | 15.7 | –14.5 | 4.4 | 4.4 |
| WN 03 | WN | – | | | | | | | | | 3.8 | 3.9 |
| WN 04 | WN | – | | | | | | | | | 3.9 | 4.8 |
| T11 | BGI | 0.50 | 0.10 | –0.08 | 0.10 | –0.05 | 0.12 | –0.12 | 1.0 | –1.3 | 5.1 | 4.4 |
| T12 | MRN | 0.50 | 0.15 | –0.15 | 0.13 | –0.16 | 0.20 | –0.24 | 2.9 | –2.2 | 5.3 | 4.3 |
| T13 | AMT | 0.50 | 0.18 | –0.19 | 0.14 | –0.17 | 0.26 | –0.27 | 3.2 | –3.1 | 5.9 | 4.3 |
| T14 | NCR | 0.50 | 0.26 | –0.25 | 0.18 | –0.20 | 0.44 | –0.42 | 9.7 | –10.8 | 4.0 | 3.4 |
| T15 ^a | AQV | 0.50 | 0.31 | –0.31 | 0.13 | –0.20 | 0.55 | –0.43 | 17.1 | –12.4 | 4.4 | 3.4 |
| WN 05 | WN | – | | | | | | | | | 3.9 | 4.1 |
| T16 | BGI | 0.75 | 0.15 | –0.10 | 0.09 | –0.11 | 0.14 | –0.14 | 1.8 | –1.5 | 4.1 | 3.7 |
| T17 | MRN | 0.75 | 0.19 | –0.19 | 0.18 | –0.23 | 0.34 | –0.34 | 5.4 | –6.7 | 5.0 | 3.5 |
| T18 | AMT | 0.75 | 0.27 | –0.30 | 0.19 | –0.24 | 0.38 | –0.37 | 5.6 | –7.3 | 4.1 | 4.0 |
| T19 | NCR | 0.75 | 0.45 | –0.40 | 0.20 | –0.29 | 0.55 | –0.57 | 26.1 | –25.0 | 2.8 | 2.3 |
| T20 | AQV | 0.75 | 0.53 | –0.49 | 0.23 | –0.27 | 0.76 | –0.61 | 30.3 | –23.1 | 2.4 | 2.4 |
| WN 06 | WN | – | | | | | | | | | 4.6 | 4.6 |
| T21 | BGI | 1.00 | 0.19 | –0.12 | 0.13 | –0.11 | 0.25 | –0.19 | 3.7 | –3.3 | 2.7 | 2.8 |
| T22 | MRN | 1.00 | 0.28 | –0.27 | 0.24 | –0.28 | 0.34 | –0.37 | 9.1 | –12.5 | 2.9 | 3.6 |
| T23 | AMT | 1.00 | 0.39 | –0.35 | 0.26 | –0.31 | 0.53 | –0.68 | 34.1 | –39.9 | 2.4 | 3.1 |
| T24 | NCR | 1.00 | 0.52 | –0.52 | 0.31 | –0.40 | 0.63 | –0.61 | 34.0 | –26.5 | 1.9 | 1.9 |
| T25 | AQV | 1.00 | 0.71 | –0.62 | 0.28 | –0.41 | 1.04 | –0.88 | 49.1 | –130.2 | 0.8 | 2.0 |
| WN 07 | WN | – | | | | | | | | | 3.4 | 3.4 |
| T26 | BGI | 1.25 | 0.23 | –0.17 | 0.15 | –0.11 | 0.22 | –0.30 | 7.1 | –7.3 | 2.6 | 2.8 |
| T27 | MRN | 1.25 | 0.35 | –0.36 | 0.30 | –0.36 | 0.46 | –0.57 | 29.1 | –33.6 | 2.0 | 2.9 |
| T28 | AMT | 1.25 | 0.46 | –0.46 | 0.37 | –0.36 | 0.59 | –0.85 | 89.5 | –83.4 | 1.3 | 1.5 |
| T29 | NCR | 1.25 | 0.76 | –0.68 | 0.31 | –0.41 | 0.74 | –0.95 | 55.9 | –80.2 | 1.1 | 0.9 |
| T30 ^b | AQV | 1.25 | 0.86 | –0.63 | 0.31 | –0.39 | 1.05 | –0.91 | 75.3 | –97.9 | 1.1 | 1.0 |
| WN 08 | WN | – | | | | | | | | | 2.8 | 2.8 |
| T31 ^c | AQV | 1.25 | 0.82 | –0.82 | 0.48 | –0.90 | 1.06 | –0.64 | 112.8 | –49.2 | 0.5 | 0.9 |

^aDevelopment of the first hinge at $z = 2.60$ m^bDevelopment of the second hinge at $z = 3.09$ m^cCollapse^dHorizontal out-of-plane displacement measured by the marker at $z = 2.46$ m (the closest to the hinge)

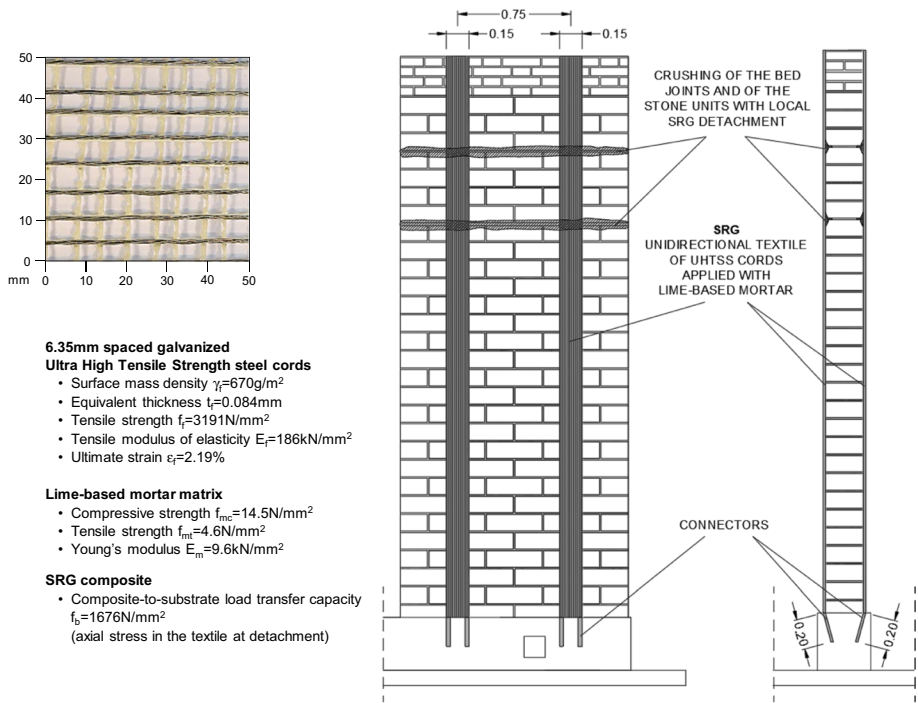


Fig. 5 Retrofitting design of the tuff wall with SRG and damage pattern at the end of tests

that the wall, at failure, was not expected to exhibit disaggregation, by virtue of the regular arrangement of the masonry, made of squared tuff blocks. For this reason, it was considered unnecessary to apply the reinforcement onto the entire surface of the wall. Moreover, since the wall was made of only one leaf, leaf separation could not occur and, therefore, no transversal connectors were installed. On the other hand, SRG connectors were installed in the reinforced concrete foundation to prevent the end debonding of the composite strips (see the following section for details on the connectors).

4.2.2 Installation phases

First, the tuff substrate was consolidated with potassium silicate and the crushed bed joints were repointed with lime-based grout. Then, the first 5 mm thick layer of matrix was laid down by hand (Fig. 6a) and the steel textile was installed taking care of letting the mortar passing through the voids between the cords (Fig. 6b). Finally, the second layer of mortar was laid down. The total thickness of the SRG strip was about 10 mm. Each strip was connected to the foundation with a 150 mm long steel connector, made by rolling the textile, inserted in a hole having 30 mm diameter, 250 mm length and about 20° inclination angle with the vertical (Fig. 6c). The hole was injected with a lime-based grout, whose mechanical properties are similar to those of the mortar matrix, but it is more fluid to make it suitable for injections. Technical information provided by the supplier reports a pull-out strength of the connector of 1 kN/cm, which, in this case, yields to 25 kN, corresponding to about 60% of the tensile strength of the 150 mm wide strip, whereas it is 15% higher than

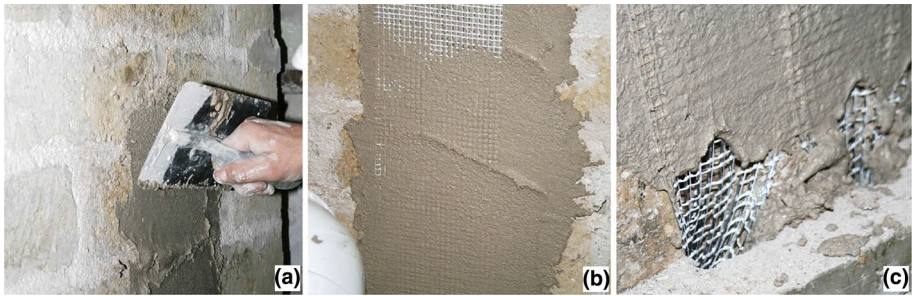


Fig. 6 Retrofitting of the tuff wall with SRG: laying of the first mortar layer (a), installation of the steel textile (b) and steel connectors inserted in the reinforced concrete foundation (c)

its bond strength on the tuff masonry substrate. This means that debonding was expected to precede pull-out. The specimen was kept wet for the first 24 h and then stored in the laboratory for 5 weeks before testing.

4.3 Response of the reinforced specimen and comparisons

4.3.1 Seismic capacity and acceleration versus displacement curves

After repair and retrofitting, the specimen was tested again on the shake table under the same input signals applied in the first session. A total of 41 seismic tests were carried out on the strengthened wall, with SF ranging from 0.50 to 2.50 (see Table 3). SRG did not significantly change the initial behaviour of the wall in terms of displacements and stiffness, but limited its out-of-plane deflections under medium–high intensity signals, as shown in Fig. 7, in which the response under the (nominally) same input signal (AQV, SF=1.25) is represented as sake of example. A combined failure mode was detected at the end of the tests, characterized by the crushing of the tuff in the same joints where the hinges had formed in the previous tests (Fig. 8a) and by the local detachment of the SRG from the crushed units (Fig. 8b). The connectors in the foundation did not show any sign of pull-out (Fig. 8c). In terms of seismic capacity, the maximum (absolute) value of a_h was 2.05 g, which is 238% of that of the unreinforced wall, whereas the distributed acceleration increased by 120% (2.33 g vs. 1.06 g), as shown by the acceleration versus displacement curves in Fig. 4.

4.3.2 Deflection profiles

Thanks to the possibility of monitoring a large number of markers, 3DVision provided information on the displacements at different heights in each time instant. Figure 9 shows the deflection profiles recorded during the last set of tests of the first test session (unreinforced specimen, Fig. 9a), during the same set of tests (same SF) but in the second test session (reinforced specimen, Fig. 9b), and, finally, during the last set of tests of the second test session (Fig. 9c). In each plot, five profiles are shown, one for each seismic input, for both positive (forwards) and negative (backwards) displacements. Each profile is built by connecting the out-of-plane horizontal displacements of the markers glued in the middle of the front side of the wall, along its height. More specifically,

Table 3 Results of the tests on the reinforced tuff wall

| Test | Signal | SF | $a_{h,max}$ | $a_{h,min}$ | $a_{v,max}$ | $a_{v,min}$ | $a_{distr,max}$ | $a_{distr,min}$ | δ_{max}^b | δ_{min}^b | f_{SISO} | f_{MIMO} |
|-------|--------|------|-------------|-------------|-------------|-------------|-----------------|-----------------|------------------|------------------|------------|------------|
| | | – | g | g | g | g | g | g | mm | mm | Hz | Hz |
| WN 01 | WN | – | | | | | | | | | 8.4 | 7.8 |
| T01 | BGI | 0.50 | 0.10 | –0.10 | 0.06 | –0.07 | 0.12 | –0.13 | 0.8 | –0.7 | 8.2 | 7.8 |
| T02 | MRN | 0.50 | 0.13 | –0.15 | 0.16 | –0.17 | 0.22 | –0.23 | 1.1 | –0.6 | 7.5 | 6.7 |
| T03 | AMT | 0.50 | 0.20 | –0.26 | 0.16 | –0.16 | 0.27 | –0.26 | 1.1 | –1.1 | 7.2 | 6.6 |
| T04 | NCR | 0.50 | 0.32 | –0.29 | 0.23 | –0.23 | 0.46 | –0.48 | 0.9 | –2.0 | 6.4 | 6.4 |
| T05 | AQV | 0.50 | 0.33 | –0.33 | 0.18 | –0.18 | 0.43 | –0.43 | 1.3 | –1.9 | 6.4 | 5.4 |
| WN 02 | WN | – | | | | | | | | | 7.2 | 7.0 |
| T06 | BGI | 0.75 | 0.16 | –0.11 | 0.09 | –0.09 | 0.18 | –0.14 | 0.7 | –1.0 | 7.2 | 7.0 |
| T07 | MRN | 0.75 | 0.22 | –0.21 | 0.19 | –0.21 | 0.26 | –0.27 | 1.0 | –1.2 | 6.5 | 6.2 |
| T08 | AMT | 0.75 | 0.28 | –0.35 | 0.20 | –0.26 | 0.40 | –0.39 | 1.8 | –2.2 | 6.4 | 6.0 |
| T09 | NCR | 0.75 | 0.55 | –0.59 | 0.26 | –0.34 | 0.68 | –0.61 | 1.2 | –3.9 | 5.4 | 5.8 |
| T10 | AQV | 0.75 | 0.53 | –0.53 | 0.30 | –0.30 | 0.64 | –0.64 | 2.8 | –4.7 | 5.4 | 5.5 |
| WN 03 | WN | – | | | | | | | | | 6.9 | 6.3 |
| T11 | BGI | 1.00 | 0.20 | –0.13 | 0.11 | –0.11 | 0.24 | –0.29 | 1.2 | –1.3 | 5.5 | 5.6 |
| T12 | MRN | 1.00 | 0.31 | –0.30 | 0.26 | –0.36 | 0.39 | –0.41 | 1.9 | –2.8 | 5.6 | 5.4 |
| T13 | AMT | 1.00 | 0.32 | –0.38 | 0.27 | –0.29 | 0.45 | –0.46 | 2.2 | –3.7 | 5.0 | 5.2 |
| T14 | NCR | 1.00 | 0.89 | –0.63 | 0.39 | –0.39 | 0.98 | –0.79 | 8.1 | –5.4 | 5.2 | 4.2 |
| T15 | AQV | 1.00 | 0.64 | –0.79 | 0.27 | –0.26 | 0.77 | –0.81 | 6.2 | –5.8 | 4.7 | 4.1 |
| WN 04 | WN | – | | | | | | | | | 5.3 | 5.0 |
| WN 05 | WN | – | | | | | | | | | 5.2 | 5.0 |
| T16 | BGI | 1.25 | 0.21 | –0.16 | 0.14 | –0.13 | 0.23 | –0.36 | 2.6 | –2.8 | 4.7 | 4.6 |
| T17 | MRN | 1.25 | 0.36 | –0.38 | 0.30 | –0.42 | 0.48 | –0.47 | 4.3 | –5.0 | 4.6 | 4.3 |
| T18 | AMT | 1.25 | 0.62 | –0.55 | 0.31 | –0.34 | 0.68 | –0.70 | 11.6 | –15.7 | 4.5 | 4.1 |
| T19 | NCR | 1.25 | 0.87 | –0.72 | 0.36 | –0.52 | 1.07 | –1.09 | 11.6 | –15.7 | 3.8 | 4.1 |
| T20 | AQV | 1.25 | 1.13 | –0.97 | 0.33 | –0.40 | 1.19 | –1.25 | 14.6 | –20.0 | 3.5 | 3.7 |
| WN 06 | WN | – | | | | | | | | | 4.1 | 4.3 |
| T21 | BGI | 1.50 | 0.29 | –0.22 | 0.18 | –0.20 | 0.23 | –0.29 | 3.5 | –3.5 | 4.2 | 4.3 |
| T22 | MRN | 1.50 | 0.43 | –0.40 | 0.35 | –0.46 | 0.60 | –0.62 | 5.7 | –6.6 | 4.0 | 4.2 |
| T23 | AMT | 1.50 | 0.64 | –0.58 | 0.42 | –0.43 | 0.68 | –0.69 | 13.8 | –16.7 | 4.0 | 3.8 |
| T24 | NCR | 1.50 | 1.13 | –0.89 | 0.37 | –0.51 | 1.40 | –1.49 | 27.3 | –29.9 | 3.2 | 3.6 |
| T25 | AQV | 1.50 | 1.29 | –0.98 | 0.36 | –0.51 | 1.39 | –1.14 | 21.9 | –18.9 | 2.9 | 3.6 |
| WN 07 | WN | – | | | | | | | | | 3.9 | 3.2 |
| T26 | BGI | 1.75 | 0.32 | –0.22 | 0.21 | –0.19 | 0.41 | –0.31 | 4.8 | –4.1 | 2.6 | 4.3 |
| T27 | MRN | 1.75 | 0.53 | –0.44 | 0.42 | –0.52 | 0.74 | –0.68 | 16.0 | –16.6 | 3.0 | 4.7 |
| T28 | AMT | 1.75 | 0.67 | –0.62 | 0.46 | –0.46 | 1.04 | –0.99 | 16.0 | –17.0 | 2.3 | 3.8 |
| WN 08 | WN | – | | | | | | | | | 3.9 | 3.1 |
| T29 | NCR | 1.75 | 1.25 | –1.02 | 0.45 | –0.60 | 1.76 | –1.71 | 36.9 | –35.5 | 2.2 | 3.5 |
| T30 | AQV | 1.75 | 1.48 | –1.45 | 0.41 | –0.54 | 1.67 | –1.46 | 23.5 | –25.0 | 2.2 | 3.7 |
| WN 09 | WN | – | | | | | | | | | 3.0 | 2.7 |
| T31 | BGI | 2.00 | 0.35 | –0.24 | 0.28 | –0.18 | 0.44 | –0.47 | 7.6 | –6.6 | 2.4 | 3.9 |
| T32 | MRN | 2.00 | 0.49 | –0.49 | 0.46 | –0.57 | 0.64 | –0.62 | 17.4 | –18.3 | 2.7 | 2.9 |
| T33 | AMT | 2.00 | 0.71 | –0.81 | 0.53 | –0.78 | 1.11 | –1.05 | 17.8 | –23.2 | 2.2 | 3.1 |
| T34 | NCR | 2.00 | 1.34 | –1.21 | 0.46 | –0.62 | 1.83 | –1.79 | 38.9 | –36.2 | 2.3 | 2.3 |

Table 3 (continued)

| Test | Signal | SF | $a_{h,max}$ | $a_{h,min}$ | $a_{v,max}$ | $a_{v,min}$ | $a_{distr,max}$ | $a_{distr,min}$ | δ_{max}^b | δ_{min}^b | f_{SISO} | f_{MIMO} |
|------------------|--------|------|-------------|-------------|-------------|-------------|-----------------|-----------------|------------------|------------------|------------|------------|
| | | – | g | g | g | g | g | g | mm | mm | Hz | Hz |
| T35 | AQV | 2.00 | 1.49 | –1.51 | 0.53 | –0.73 | 1.71 | –1.91 | 35.4 | –38.7 | 2.0 | 2.1 |
| WN 10 | WN | – | | | | | | | | | 2.5 | 2.2 |
| T36 | MRN | 2.25 | 0.61 | –0.64 | 0.50 | –0.69 | 0.89 | –0.78 | 17.8 | –19.8 | 2.7 | 2.2 |
| T37 | AMT | 2.25 | 0.96 | –0.83 | 0.59 | –0.67 | 1.08 | –1.12 | 28.2 | –30.0 | 2.4 | 2.0 |
| T38 | NCR | 2.25 | 1.55 | –1.29 | 0.56 | –0.70 | 1.72 | –1.73 | 42.7 | –43.2 | 1.9 | 2.0 |
| T39 | AQV | 2.25 | 1.66 | –1.65 | 1.35 | –1.27 | 1.72 | –2.04 | 45.6 | –47.1 | 1.9 | 1.9 |
| WN 11 | WN | – | | | | | | | | | 2.3 | 2.0 |
| T40 | NCR | 2.50 | 1.78 | –1.54 | 0.52 | –0.74 | 1.96 | –2.33 | 63.8 | –58.2 | 1.9 | 1.9 |
| T41 ^a | AQV | 2.50 | 2.05 | –1.81 | 0.60 | –0.98 | 2.15 | –1.91 | 110.1 | –63.5 | 1.8 | 1.7 |
| WN 12 | WN | – | | | | | | | | | 2.2 | 1.8 |

^aCollapse

^bHorizontal out-of-plane displacement measured by the marker at $z=2.46$ m

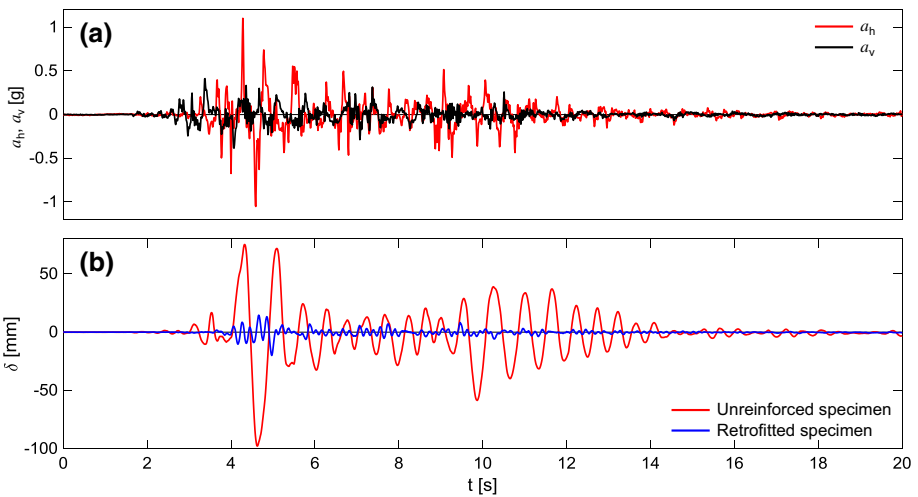


Fig. 7 Acceleration recorded on the foundation and out-of-plane horizontal displacement (measured by 3DVision on the marker at $z=2.46$ m) on the tuff wall (before and after retrofiting) under AQV signal with SF=1.25

the first marker (at $z=0$) was on the foundation, six markers were on the masonry wall (at $z=1.01$ m, $z=1.78$ m, $z=2.37$ m, $z=2.46$ m, $z=2.81$ m, $z=3.17$ m) and the last one ($z=3.49$ m) was on the top beam. The deflection profiles are represented in the time instant of the maximum (δ_{max}) and minimum (δ_{min}) displacements of the marker at $z=2.46$ m, which was the closest one to the first hinge (developed after T15 in the first test session), already used in previous analyses (Figs. 4, 7). Note that, since SRG reinforcement reduced the maximum displacements of the wall under comparable input intensity, a different scale was used in Fig. 9b with respect to Fig. 9a, c.

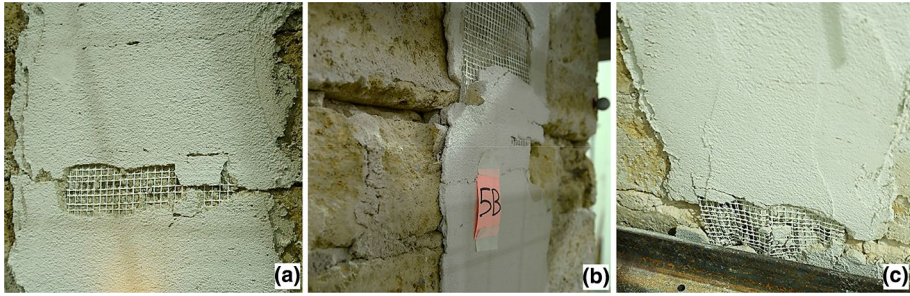


Fig. 8 Damage pattern of the reinforced tuff wall at the end of the shake table test session: cracking of the mortar matrix (a), crushing of the tuff units (b) and connector in the foundation (c)

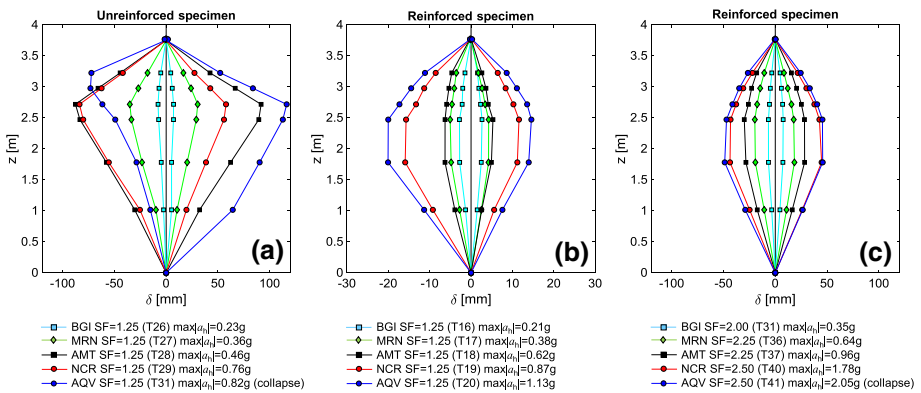


Fig. 9 Deflection profiles of the tuff wall before (a) and after (b, c) SRG retrofitting

The deflection profiles show that the response of the unreinforced wall was mainly governed by the development of a hinge in the middle, in addition to the one at the base and to the top constrain provided by the rollers, and can therefore be assimilated to that of a system of two nearly-rigid blocks. The only exception is the profile of the last test (T31, Fig. 9a) in which the development of the second intermediate hinge is clearly visible in the negative side (backwards deflection), so the wall behaved as a three-block mechanism. The profiles of the retrofitted wall, apart from the smaller displacements, show a wider deflection distribution. In this case, due to the tensile strength provided by SRG, the response was similar to a nearly-elastic beam, simply supported at the base (where the SRG strips did not prevented rotation) and on top (due to the presence of the rubber rollers whose effect was not affected by the retrofitting work).

4.3.3 Dynamic properties and damage accumulation

The fundamental frequency of the wall (f) was calculated through the transfer function between the acceleration time-histories recorded by the sensors on the wall (output signals) and on the foundation (input signals). The transfer function, which is calculated as the cross power spectral density of the input and the output signals divided by the power spectral

density of the input signal, provides information on the filter effect of the structure on the seismic input received at its base and can be used for dynamic identification under both stationary (white noise) and non-stationary (seismic) input signals. In this case, for the seismic tests, data acquisition was prolonged for 30 s after the end of the input and dynamic identification analyses were based only on the data recorded in these last 30 s of free vibrations. Clearly, the amplitude of the accelerations tended to reduce during the free vibrations due to damping, but it was verified that, even after low-intensity inputs, the amplitude of recorded acceleration was out of the sensitivity range of the instruments.

Two experimental modal analyses methods were used, namely a Single-Input/Single-Output (SISO) approach and a Multi-Input/Multi-Output (MIMO) approach. In the former, the horizontal acceleration recorded by the accelerometer on the foundation (A2) was used as input signal and that of the accelerometer on the wall near the hinge (A7) was used as output signal. In the latter, the data provided by 3DVision were used. First, the horizontal component (in the out-of-plane direction) of the displacement time-histories of the markers were derived two times to obtain acceleration time-histories. Then, the average of the accelerations of the markers on the foundation and on the shake table was taken as input signal and that of the markers on the upper half of the wall (excluding the top beam) was taken as output signal. In principle, thanks to the use of a large number of input and output points, the MIMO approach should provide smoother and more stable (less noisy) results than the SISO one, which, on the other hand, requires less efforts in setup implementation and data analysis (Maia and Silva 1998).

Figure 10a shows the values of f provided by the two methods (SISO and MIMO) in the two shake table test sessions in sequence. In the unreinforced specimen (Table 2), the frequency decreased from 8.1–8.2 Hz (WN01) to 0.9–1.1 Hz (T29–T31). The repair and retrofitting works almost restored the initial frequency (Table 3, WN01), indicating that both the (localized) repointing of the cracked joints and the installation of the SRG strips compensated for the effect of the (more distributed) damage developed in the first test session. The presence of the SRG reinforcement, also led to a slower damage accumulation with respect to the unreinforced specimen. In the last test (T41), f was 1.7–1.8 Hz, which is slightly higher than that recorded at the end of the former test series, but it was reached after a longer session with much higher intensities.

From a methodological standpoint, SISO and MIMO methods provided similar frequencies (which validated both the results and the methods) and the frequency calculated in WN tests (represented by white markers in Fig. 10) was, as a general trend, 10–30% higher than in seismic tests, which might be due to the smaller amplitude of oscillations.

With the aim of representing the accumulation of damage, a damage index (DI) was calculated starting from the frequencies provided by SISO and MIMO approaches using the expression in Eq. (1), in which f_i is the frequency of the i -th test and f_1 is that of the first test, taken as reference for the initial (undamaged) state (Mendes et al. 2014). DI, by definition, is null for the first test and tends to 1 with the increase of damage (it would be 1 for $f_i=0$), and its variation reflects that of f , as shown in Fig. 10b.

$$DI_i = 1 - \left(\frac{f_i}{f_1} \right)^2 \quad (1)$$

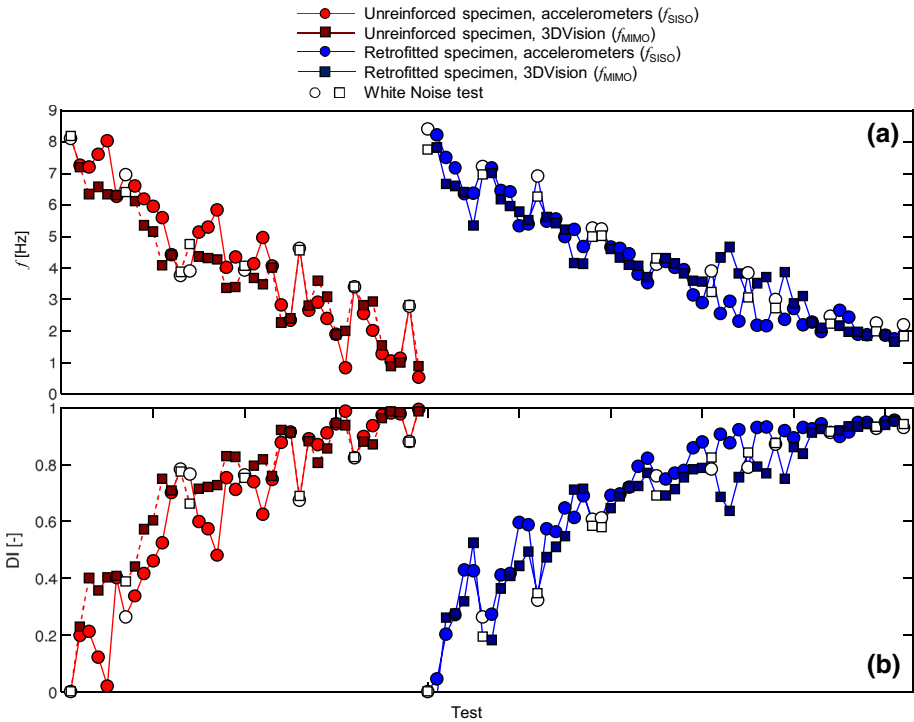


Fig. 10 Fundamental frequency (a) and damage index (b) of the tuff wall

5 Seismic behaviour of the stone wall

5.1 Response of the unreinforced specimen

Being built on the same foundation, the stone wall underwent the same sequence of shake table tests of the tuff wall. In this case, the mortar joint at $z=2.54$ m crushed at the end of the series with $SF=0.25$. The presence of horizontal joints facilitated the development of such horizontal hinge, whereas the headers prevented leaf separation. From this moment on, the wall behaved as a two-block mechanism. In test T20, performed under AQV signal with $SF=0.75$, both the maximum acceleration ($a_{h,max}=0.53$ g) and the maximum displacement ($\delta=-134.4$ mm, the negative sign meaning that it was backwards) of the test session were recorded (Fig. 11). The displacement was measured on the marker at $z=2.31$ m, which was the closest one to the hinge. The wall was considered collapsed (Table 4), and the steel frames hinged to the foundation were closed to block it and avoid further damage or fall of stone units on the shake table. This allowed the tests to be continued on the tuff wall.

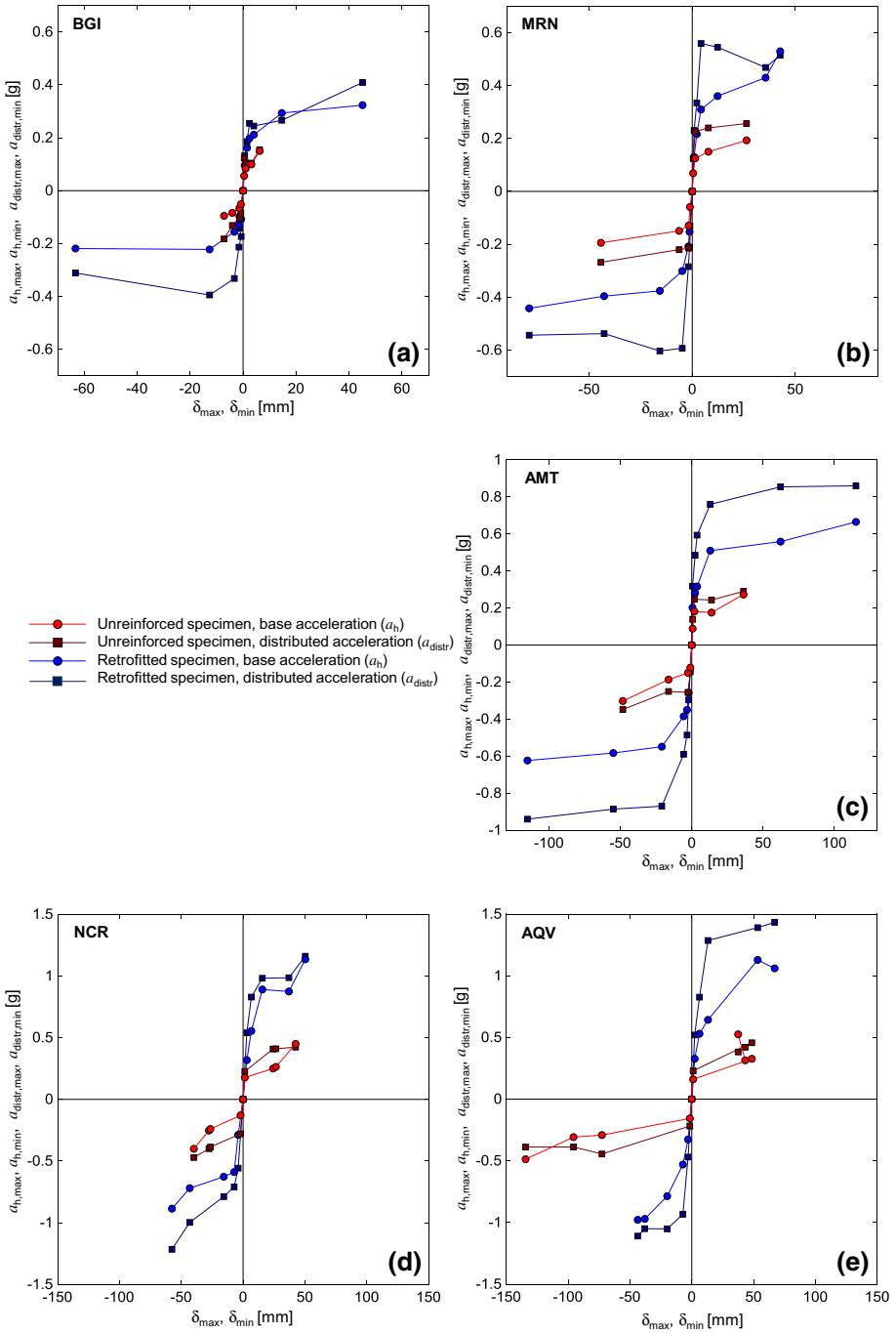


Fig. 11 Base and distributed acceleration versus displacement curves of the stone specimen before and after BTRM retrofitting under BGI (a), MRN (b), AMT (c), NCR (d) and AQV (e) seismic inputs

Table 4 Results of the tests on the unreinforced stone wall

| Test | Signal | SF | $a_{h,max}$ | $a_{h,min}$ | $a_{v,max}$ | $a_{v,min}$ | $a_{distr,max}$ | $a_{distr,min}$ | δ_{max}^c | δ_{min}^c | f_{SISO} | f_{MIMO} |
|------------------|--------|------|-------------|-------------|-------------|-------------|-----------------|-----------------|------------------|------------------|------------|------------|
| | | – | g | g | g | g | g | g | mm | mm | Hz | Hz |
| WN 01 | WN | – | | | | | | | | | 8.1 | 7.9 |
| T01 | BGI | 0.25 | 0.06 | –0.05 | 0.05 | –0.04 | 0.12 | –0.08 | 0.4 | –0.8 | 7.6 | 8.3 |
| T02 | MRN | 0.25 | 0.07 | –0.06 | 0.08 | –0.08 | 0.12 | –0.13 | 0.5 | –1.1 | 7.6 | 7.0 |
| T03 | AMT | 0.25 | 0.09 | –0.12 | 0.07 | –0.09 | 0.14 | –0.14 | 0.6 | –1.0 | 7.6 | 7.6 |
| T04 | NCR | 0.25 | 0.18 | –0.13 | 0.10 | –0.10 | 0.23 | –0.28 | 1.4 | –2.1 | 6.3 | 6.3 |
| T05 ^a | AQV | 0.25 | 0.16 | –0.16 | 0.10 | –0.11 | 0.23 | –0.22 | 1.1 | –1.6 | 6.3 | 6.8 |
| WN 02 | WN | – | | | | | | | | | 7.0 | 6.8 |
| T06 | BGI | 0.50 | 0.08 | –0.07 | 0.06 | –0.06 | 0.11 | –0.10 | 1.0 | –1.4 | 6.8 | 6.8 |
| T07 | MRN | 0.50 | 0.13 | –0.13 | 0.12 | –0.16 | 0.23 | –0.21 | 1.5 | –1.7 | 6.4 | 6.1 |
| T08 | AMT | 0.50 | 0.18 | –0.15 | 0.13 | –0.16 | 0.25 | –0.26 | 1.9 | –2.6 | 6.1 | 6.0 |
| T09 | NCR | 0.50 | 0.25 | –0.24 | 0.15 | –0.24 | 0.41 | –0.39 | 24.3 | –26.4 | 3.9 | 4.0 |
| T10 | AQV | 0.50 | 0.33 | –0.29 | 0.13 | –0.23 | 0.46 | –0.44 | 33.4 | –45.5 | 4.0 | 3.0 |
| WN 03 | WN | – | | | | | | | | | 3.8 | 3.9 |
| WN 04 | WN | – | | | | | | | | | 3.9 | 4.0 |
| T11 | BGI | 0.50 | 0.10 | –0.08 | 0.10 | –0.05 | 0.10 | –0.13 | 3.1 | –4.1 | 3.8 | 3.8 |
| T12 | MRN | 0.50 | 0.15 | –0.15 | 0.13 | –0.16 | 0.24 | –0.22 | 7.8 | –6.4 | 3.6 | 3.6 |
| T13 | AMT | 0.50 | 0.18 | –0.19 | 0.14 | –0.17 | 0.24 | –0.25 | 13.8 | –16.3 | 2.9 | 3.0 |
| T14 | NCR | 0.50 | 0.26 | –0.25 | 0.18 | –0.20 | 0.41 | –0.40 | 26.5 | –27.6 | 1.9 | 2.3 |
| T15 | AQV | 0.50 | 0.31 | –0.31 | 0.13 | –0.20 | 0.42 | –0.39 | 43.2 | –95.6 | 2.0 | 2.0 |
| WN 05 | WN | – | | | | | | | | | 4.3 | 4.3 |
| T16 | BGI | 0.75 | 0.15 | –0.10 | 0.09 | –0.11 | 0.15 | –0.18 | 6.2 | –7.2 | 3.6 | 3.7 |
| T17 | MRN | 0.75 | 0.19 | –0.19 | 0.18 | –0.23 | 0.26 | –0.27 | 26.4 | –44.3 | 3.0 | 3.6 |
| T18 | AMT | 0.75 | 0.27 | –0.30 | 0.19 | –0.24 | 0.29 | –0.35 | 36.3 | –48.3 | 2.4 | 1.6 |
| T19 | NCR | 0.75 | 0.45 | –0.40 | 0.20 | –0.29 | 0.42 | –0.47 | 42.5 | –39.8 | 1.7 | 1.7 |
| T20 ^b | AQV | 0.75 | 0.53 | –0.49 | 0.23 | –0.27 | 0.38 | –0.39 | 37.5 | –134.4 | 1.0 | 1.0 |

^aDevelopment of the first hinge at $z = 2.54$ m

^bCollapse assumed

^cHorizontal out-of-plane displacement measured by the marker at $z = 2.31$ m (the closest to the hinge)

5.2 Strengthening with Basalt Textile Reinforced Mortar (BTRM)

5.2.1 Reinforcement materials and layout

After the tests, the stone wall was reinforced on both sides with a BTRM composite, including a bidirectional balanced basalt fabric with 8 mm×8 mm grid spacing (Fig. 12). The fibre yarns are pre-impregnated to improve adhesion and durability (Lignola et al. 2017) and each of them also includes two stainless steel micro-wires. The basalt mesh has $\gamma_f = 400$ g/m², $t_f = 0.064$ mm, $f_f = 881$ N/mm², $E_f = 51.9$ kN/mm² and $\epsilon_f = 1.92\%$; the BTRM-to-substrate load transfer capacity (axial stress in the textile at detachment) is $f_b = 580$ N/mm² (mean values, determined experimentally through laboratory tests performed before wall retrofitting). The textile was bonded to the entire surface of the wall, including the top beam, with the same lime-based mortar used for SRG.

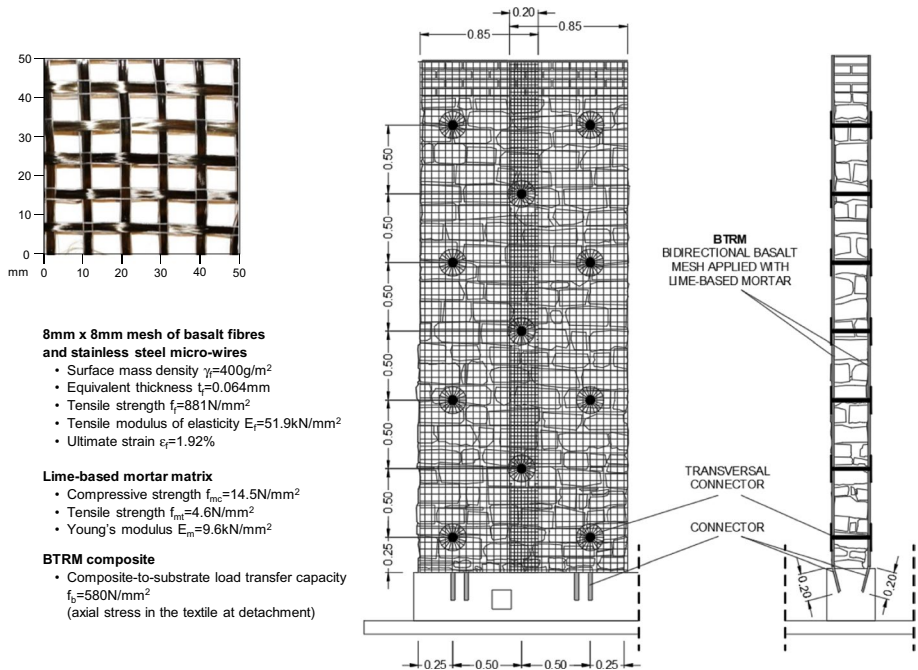


Fig. 12 Retrofitting design of the stone wall with BTRM

Since the fabric is supplied in 1 m wide sheets, two 0.85 m wide plies were installed to cover the entire surface of the wall, with a 0.2 m overlap in the middle.

Given the irregular arrangement of the stones, which had caused some local detachments in the tests on the unreinforced specimen, it was necessary to cover the entire surface of the wall. Both the cross-sectional area of fabric and the TRM-to-substrate surface were larger than those of the SRG installed on the tuff wall, so the BTRM system provided sufficient tensile and bond strength, despite its relatively lower mechanical performances. Moreover, since the wall had two leaves, transversal steel connectors (with density of $2/\text{m}^2$) were installed to prevent leaf separation and improve the substrate-to-TRM load transfer capacity. Finally, in order to prevent end debonding, the composite was connected to the reinforced concrete foundation.

5.2.2 Installation phases

First, the wall was repaired by repointing the crushed joints with lime-based grout and replacing the stones that had fallen down (Fig. 13a). The masonry was wet with water and the first layer of matrix was laid down. Then, the fabric was installed (Fig. 13b) and the top layer of mortar was laid down. The overall thickness of the TRM overlay was about 10 mm, even if the unevenness of the substrate entailed local variability. The connectors (Fig. 13c) were made by rolling the UHTSS textile used for SRG and a plastic wedge, inserted in crossing holes drilled in the masonry before the installation of the basalt mesh and injected with lime-based grout at the end of the retrofitting works. Grout injections filled the voids, providing an additional improvement of the mechanical properties of the

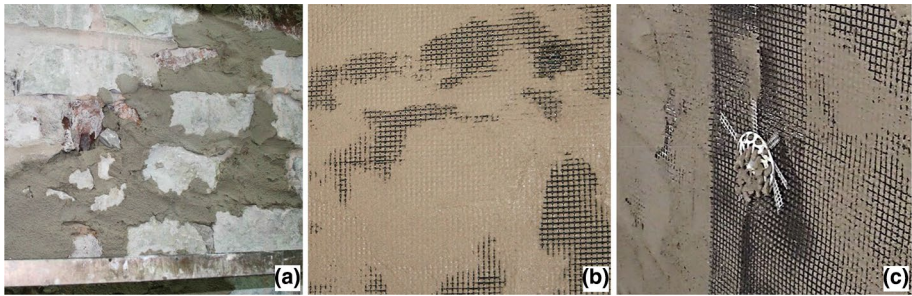


Fig. 13 Retrofitting of the stone wall with BTRM: repointing of the crushed joints (a), installation of the basalt mesh (b) and grout injection of the transversal steel connectors (c)

masonry (Giaretton et al. 2017). The lower connectors between BTRM overlay and reinforced concrete foundation were made with the same textile used for SRG. They were inserted in holes drilled in the reinforced concrete foundation and then injected with lime-based grout, as it was done for the SRG reinforcement on the tuff wall. On the other side, they were bonded over the basalt mesh with an overlap length of 200 mm. Like the tuff wall, also the stone specimen was kept wet for the first 24 h and then stored in the laboratory for 5 weeks before testing.

5.3 Response of the reinforced specimen and comparisons

5.3.1 Seismic capacity and acceleration versus displacement curves

The BTRM reinforcement entailed a gain in seismic capacity of 113%. The maximum (absolute) acceleration recorded on the foundation was $a_{h,max} = 1.13$ g during test T24 (NCR, SF=1.50, Fig. 11d). Collapse occurred during test T28 (AMT signal, SF=1.75, $a_{h,max} = 0.67$ g). As done for the tuff wall, the distributed acceleration (a_{distr}) was calculated as a further measure of the input transferred to the specimen, which is closer to the inertial forces than the sole base acceleration (a_h). A maximum value of $a_{distr,max} = 1.43$ g was calculated at test T25 (AQV, SF=1.50, Fig. 11e), which was 304% of that calculated on the unreinforced specimen ($a_{distr,min} = -0.47$ g, test T19, NCR, SF=0.75, Fig. 11d). Note that, due to dynamic amplification, the maximum base acceleration and maximum distributed acceleration were not in the same test.

The basalt mesh detached locally from the substrate during the set of tests with SF=1.0, approximately at the same height where the hinge developed in the test session on the unreinforced wall (Fig. 14a). Damage progressively developed (Fig. 14b) and, at failure, a large surface of the reinforcement debonded from the masonry substrate (Figs. 14c, 15a). Such detachment appeared caused by a combination of shear stresses and buckling of the TRM overlay. The steel connectors (Fig. 15b), however, remained effective (they did not show signs of pull-out) and, in addition to preventing leaf separation, contributed to the load transfer mechanism from the wall to the basalt fabric. Indeed, even if this latter was partially detached from the substrate, the presence of the connectors made it still effective similarly to an unbonded tendon between connectors. Finally, signs of tensile rupture of the basalt wires were detected only locally near the edges of the stones (Fig. 15c).

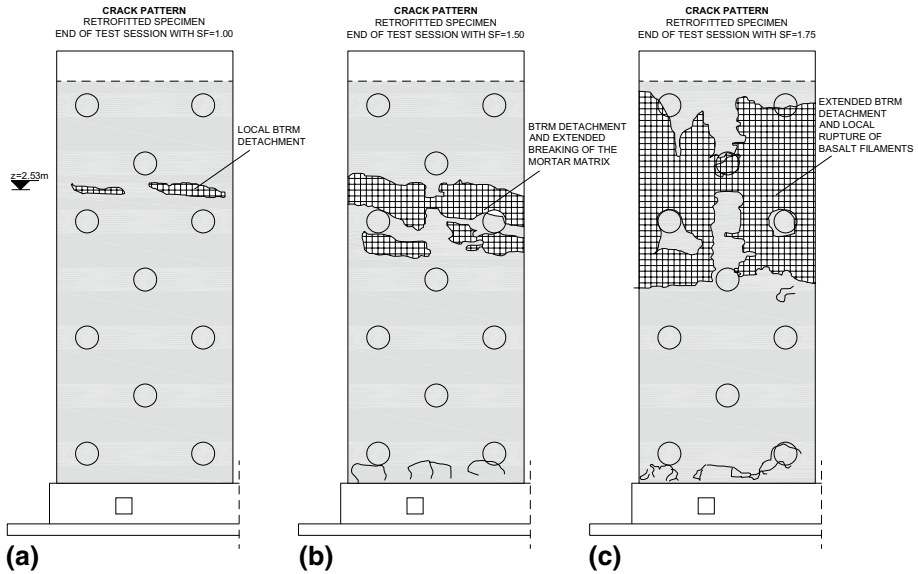


Fig. 14 Damage pattern of the retrofitted stone wall after test series with SF=1.00 (a), SF=1.50 (b) and SF=1.75 (c)



Fig. 15 Damage pattern of the reinforced stone wall at the end of the shake table test session: BTRM detachment (a), detail of the connector (b), local rupture of the basalt wires at the edges of crushed stones (c)

The gain in strength was associated with an increase of displacement, as shown by the acceleration versus displacement response curves (Fig. 11), which is clearly also due to the higher input intensity attained in the tests on the retrofitted specimen. The response in time of the same marker ($z=2.61$ m) under the same input (AQV, SF=0.75) is plotted in Fig. 16, showing the reduction of the displacements entailed by the reinforcement.

5.3.2 Deflection profiles

The deflection profiles of the stone wall, before and after retrofitting, are shown in Fig. 17. As in the case of the tuff wall, there is a marker on the foundation ($z=0$), one on the top beam ($z=3.75$ m), and six on the wall, at $z=1.04$ m, $z=1.84$ m, $z=2.36$ m, $z=2.61$ m, $z=2.98$ m

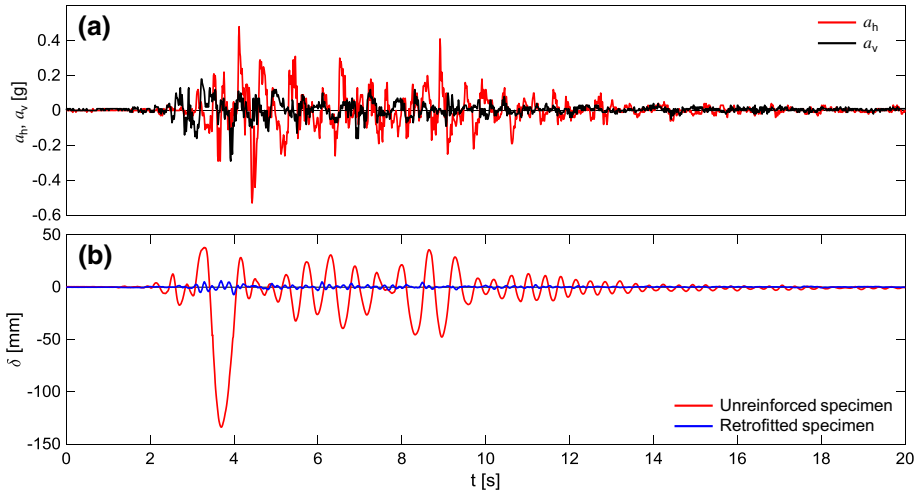


Fig. 16 Acceleration recorded on the foundation and out-of-plane horizontal displacement (measured by 3DVision on the marker at $z=2.61$ m) on the stone wall (before and after retrofiting) under AQV signal with SF=0.75

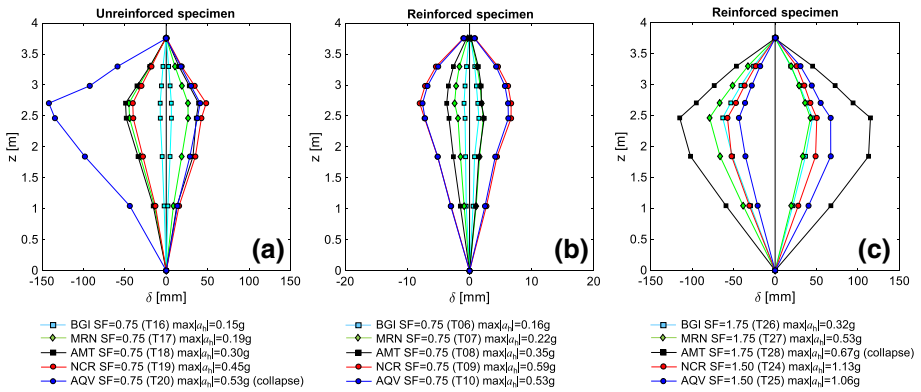


Fig. 17 Deflection profiles of the stone wall before (a) and after (b, c) BTRM retrofiting

and $z=3.30$ m. The closest marker to the hinge developed after T05 in the first test session was at $z=2.61$ m and the deflection profiles are built for each test in the time instants when this marker attained δ_{max} and δ_{min} , respectively. As for the tuff wall, also in this case the response of the unreinforced wall was mainly governed by the presence of the hinge (Fig. 17a), whereas the BTRM overlay entails both a reduction (for the same input, Fig. 17b) and a redistribution (also at collapse, Fig. 17c) of the deflections along the height of the wall.

5.3.3 Dynamic properties and damage accumulation

The fundamental frequency (f) of the unreinforced stone wall (Fig. 18a) was about 8 Hz before the beginning of the tests and suddenly decreased to 3.8–3.9 Hz after the first runs

of tests with $SF=0.50$ (see WN03 and WN04 in Table 4). At collapse, both the experimental modal analysis approaches (SISO and MIMO) provided a frequency of 1.0 Hz. The repair works and the installation of the BTRM reinforcement balanced the effect of the damage accumulated in the former test series and restored the initial frequency of the undamaged specimen ($f=7.8$ Hz, Table 5). As observed in the tuff wall, also in this case the composite overlay entailed a slower accumulation of damage, since the same reduction of stiffness (f decreased to 1.3–1.4 Hz) was obtained as the effect of more tests under higher intensity of seismic input (Fig. 18a). Finally, the increase of the damage index (DI), plotted in Fig. 18b, clearly shows both the slower accumulation of damage ensured by the BTRM and the absence of the sudden damage increases visible on the unreinforced wall.

6 Design provisions

Existing design guides (ACI 2013) and recent research studies (D’Antino et al. 2018; Meriggi et al. 2019) provide analytical relationships to estimate the ultimate flexural strength of masonry walls reinforced with TRM composites. The suggested approaches consist in a cross-sectional analysis under compression and bending, under the assumptions that plane sections remain plane and that there is strain compatibility between masonry and TRM. As for masonry, either an elastic–plastic behaviour or a stress–block diagram is assumed in compression. TRM, instead, is considered linear elastic to failure in

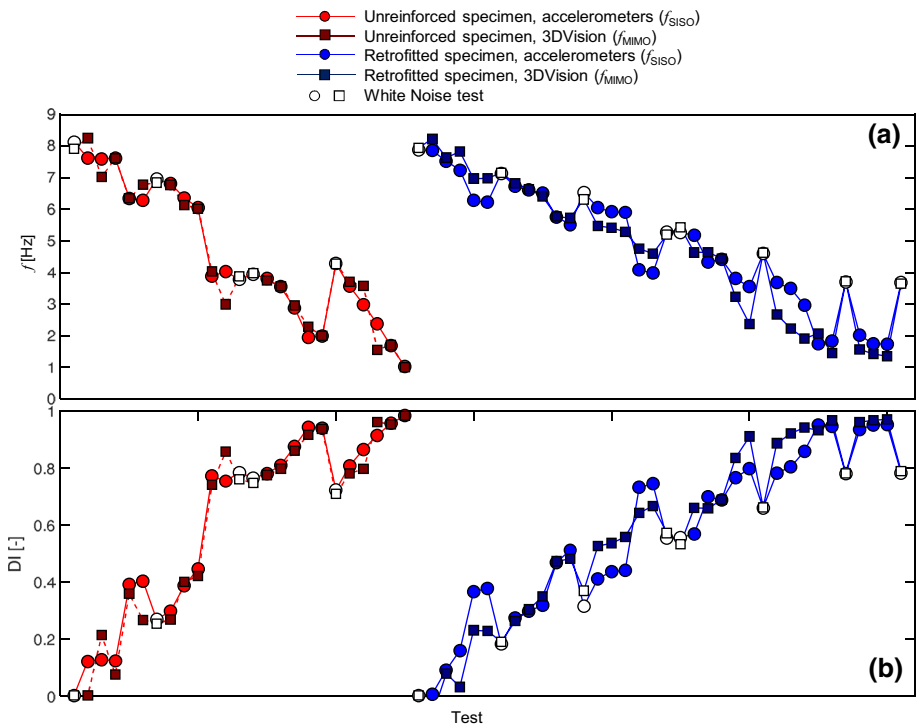


Fig. 18 Fundamental frequency (a) and damage index (b) of the stone wall

Table 5 Results of the tests on the reinforced stone wall

| Test | Signal | SF | $a_{h,max}$ | $a_{h,min}$ | $a_{v,max}$ | $a_{v,min}$ | $a_{distr,max}$ | $a_{distr,min}$ | δ_{max}^d | δ_{min}^d | f_{SISO} | f_{MIMO} |
|------------------|--------|------|-------------|-------------|-------------|-------------|-----------------|-----------------|------------------|------------------|------------|------------|
| | | – | g | g | g | g | g | g | mm | mm | Hz | Hz |
| WN 01 | WN | – | | | | | | | | | 7.9 | 7.9 |
| T01 | BGI | 0.50 | 0.10 | –0.10 | 0.05 | –0.04 | 0.13 | –0.14 | 0.6 | –1.3 | 7.9 | 8.2 |
| T02 | MRN | 0.50 | 0.13 | –0.15 | 0.14 | –0.18 | 0.23 | –0.21 | 0.9 | –1.3 | 7.5 | 7.6 |
| T03 | AMT | 0.50 | 0.20 | –0.26 | 0.16 | –0.16 | 0.32 | –0.30 | 0.5 | –2.2 | 7.2 | 7.8 |
| T04 | NCR | 0.50 | 0.32 | –0.29 | 0.23 | –0.23 | 0.54 | –0.56 | 3.0 | –4.0 | 6.3 | 7.0 |
| T05 | AQV | 0.50 | 0.33 | –0.33 | 0.18 | –0.18 | 0.52 | –0.47 | 2.4 | –3.0 | 6.2 | 7.0 |
| WN 02 | WN | – | | | | | | | | | 7.1 | 7.2 |
| T06 | BGI | 0.75 | 0.16 | –0.11 | 0.09 | –0.09 | 0.19 | –0.17 | 1.5 | –0.7 | 6.7 | 6.8 |
| T07 | MRN | 0.75 | 0.22 | –0.21 | 0.19 | –0.21 | 0.33 | –0.28 | 2.2 | –1.9 | 6.6 | 6.6 |
| T08 | AMT | 0.75 | 0.28 | –0.35 | 0.20 | –0.26 | 0.49 | –0.49 | 2.4 | –3.3 | 6.5 | 6.4 |
| T09 | NCR | 0.75 | 0.55 | –0.59 | 0.26 | –0.34 | 0.83 | –0.71 | 6.7 | –7.2 | 5.8 | 5.8 |
| T10 | AQV | 0.75 | 0.48 | –0.53 | 0.18 | –0.30 | 0.83 | –0.93 | 6.2 | –7.2 | 5.5 | 5.7 |
| WN 03 | WN | – | | | | | | | | | 6.5 | 6.3 |
| T11 | BGI | 1.00 | 0.20 | –0.13 | 0.11 | –0.11 | 0.25 | –0.21 | 2.4 | –1.6 | 6.1 | 5.5 |
| T12 | MRN | 1.00 | 0.31 | –0.30 | 0.26 | –0.36 | 0.56 | –0.59 | 4.3 | –4.9 | 5.9 | 5.4 |
| T13 | AMT | 1.00 | 0.32 | –0.38 | 0.27 | –0.29 | 0.59 | –0.59 | 3.7 | –5.7 | 5.9 | 5.3 |
| T14 | NCR | 1.00 | 0.89 | –0.63 | 0.39 | –0.39 | 0.98 | –0.79 | 15.5 | –15.6 | 4.1 | 4.8 |
| T15 ^a | AQV | 1.00 | 0.64 | –0.79 | 0.27 | –0.26 | 1.29 | –1.05 | 13.1 | –19.8 | 4.0 | 4.6 |
| WN 04 | WN | – | | | | | | | | | 5.3 | 5.2 |
| WN 05 | WN | – | | | | | | | | | 5.3 | 5.4 |
| T16 | BGI | 1.25 | 0.21 | –0.16 | 0.14 | –0.13 | 0.24 | –0.33 | 4.0 | –3.3 | 5.2 | 4.6 |
| T17 | MRN | 1.25 | 0.36 | –0.38 | 0.30 | –0.42 | 0.55 | –0.60 | 12.3 | –15.7 | 4.3 | 4.6 |
| T18 | AMT | 1.25 | 0.51 | –0.55 | 0.31 | –0.34 | 0.76 | –0.87 | 12.9 | –21.0 | 4.4 | 4.4 |
| T19 | NCR | 1.25 | 0.87 | –0.72 | 0.36 | –0.52 | 0.99 | –1.00 | 37.1 | –43.2 | 3.8 | 3.2 |
| T20 | AQV | 1.25 | 1.13 | –0.97 | 0.33 | –0.40 | 1.39 | –1.05 | 53.3 | –38.0 | 3.6 | 2.4 |
| WN 06 | WN | – | | | | | | | | | 4.6 | 4.6 |
| T21 | BGI | 1.50 | 0.29 | –0.22 | 0.18 | –0.20 | 0.27 | –0.39 | 14.6 | –12.6 | 3.7 | 2.7 |
| T22 | MRN | 1.50 | 0.43 | –0.40 | 0.35 | –0.46 | 0.47 | –0.54 | 35.6 | –42.8 | 3.5 | 2.2 |
| T23 | AMT | 1.50 | 0.56 | –0.58 | 0.42 | –0.43 | 0.85 | –0.89 | 62.2 | –55.0 | 3.0 | 1.9 |
| T24 | NCR | 1.50 | 1.13 | –0.89 | 0.37 | –0.51 | 1.16 | –1.22 | 50.3 | –57.5 | 1.7 | 2.1 |
| T25 ^b | AQV | 1.50 | 1.06 | –0.98 | 0.36 | –0.51 | 1.43 | –1.11 | 67.0 | –43.7 | 1.8 | 1.5 |
| WN 07 | WN | – | | | | | | | | | 3.7 | 3.7 |
| T26 | BGI | 1.75 | 0.32 | –0.22 | 0.21 | –0.19 | 0.41 | –0.31 | 45.1 | –63.3 | 2.0 | 1.6 |
| T27 | MRN | 1.75 | 0.53 | –0.44 | 0.42 | –0.52 | 0.52 | –0.54 | 42.7 | –79.1 | 1.7 | 1.4 |
| T28 ^c | AMT | 1.75 | 0.67 | –0.62 | 0.46 | –0.46 | 0.86 | –0.94 | 115.1 | –115.2 | 1.7 | 1.4 |
| WN 08 | WN | – | | | | | | | | | 3.7 | 3.7 |

^aLocal detachment of the BTRM reinforcement

^bExtended breaking of the mortar matrix

^cCollapse

^dHorizontal out-of-plane displacement measured by the marker at z=2.61 m

tension, whereas its contribution in compression is neglected. TRM ultimate axial strain is determined through a qualification procedure based either on clevis gripped tensile tests on coupon specimens (ICC-ES 2016) or on the combination of TRM-to-substrate shear bond tests and clamping gripped tensile tests on bare textile specimens (De Santis et al. 2018a). According to this procedure, the failure mode, either crushing of masonry in compression or failure of the TRM reinforcement by detachment or tensile rupture, is first identified. Then, the neutral axis depth (c_u) is determined by imposing the balance of vertical force resultants (existing axial load, compression in masonry, tension in the reinforcement). Once the neutral axis depth, the strain levels in the masonry and in the reinforcement, the force resultants and their position are known, the ultimate flexural strength is calculated.

As an alternative to such strain compatibility based approach, a limit analysis based method, which expresses ultimate limit state conditions in terms of maximum stresses can be used. It neglects strain compatibility and assumes that both masonry and TRM exploit their full strength at the same time, making the identification of the failure mode unnecessary. The ultimate state of the materials is described by maximum force resultants and not by maximum strains. The yield design assumptions highly simplify equations and require only the material parameters related to tensile and compressive strength, whereas the Young's modules and the strains (which are more difficult to determine experimentally and may be more scattered than loads and stresses) are not necessary. This limit analysis based approach appears suitable for design and proved reliable at least for a preliminary assessment (Meriggi et al. 2019).

Both the methods (the strain compatibility based approach and the limit analysis based one) were validated and calibrated in Meriggi et al. (2019) on the basis of databases of quasi-static bending tests, including three/four point bending tests on medium scale panels and four point bending tests or airbag tests on full-scale wall specimens. Shake table tests were instead excluded.

In this section, the flexural strength of the two specimens tested within the present study was estimated analytically and compared to experimental results to investigate the reliability of the theoretical approaches in case of earthquake base motion. The calculation was made in the cross section that, based on the deflection profiles, experiences the highest bending moment, that is at $z=1.90$ m for the tuff wall (Fig. 9c) and at $z=2.20$ m for the stone wall (Fig. 17c). The axial load in this section was calculated considering the self-weight of the upper portion of the wall, in addition to the top beam and the steel plates, and resulted 25.2 kN for the tuff wall and 96.6 kN for the stone wall. The effect of the vertical acceleration was instead neglected. As for the mechanical properties of masonry, a stress-block diagram was used in compression, with a constant stress value of $0.85f_c$ over a depth of $0.8c_u$, f_c being the compressive strength (5.9 N/mm² for the tuff masonry and 14.3 N/mm² for the stone masonry, see §3.1). A ultimate strain of 0.0035 was considered (CEN 2016). As for SRG and BTRM composites, the ultimate strain values were determined as $\epsilon_d = 1.5f_b/E_f$ (De Santis et al. 2018a), where f_b is the TRM-to-substrate shear bond strength and E_f is the Young's modulus of the dry textile, reported in §4.2.1 for SRG and in §5.2.1 for the BTRM. The coefficient of 1.5 was taken considering that failure was expected to occur by intermediate detachment from the substrate (Meriggi et al. 2019). Clearly, average mechanical properties were considered and no partial safety factors were applied, and the resulting ultimate strain was 0.013 for SRG and 0.017 for BTRM. As for the tuff wall, the ultimate flexural strength estimated through the strain compatibility based approach was 16.9 kNm and the predicted failure mode was TRM detachment, whereas the limit analysis based approach provided a strength of 17.4 kNm. The wall was considered as a simply supported beam, the constraints being the lower crack at the base (first mortar bed joint) and

the rubber hollow cylinders on top (Fig. 2). Either a uniform or a segmental horizontal load distributions were assumed. The former (uniform) was equal to the maximum base acceleration ($\max|a_h|$, see §4.3.1) multiplied by the weight density (γ). The latter (segmental) was determined as the acceleration profile built from the data of the accelerometers (already used to calculate a_{distr}) multiplied by the weight density (γ), with the aim of accounting for the dynamic amplification over the height of the wall, although in a simplified way. The external bending moment resulted 16.5 kNm under the uniform horizontal load distribution and 19.7 kNm under the segmental one.

The theoretical ultimate flexural strength of the stone wall was 23.2 kNm with a strain compatibility based approach (also in this case the predicted failure mode was TRM detachment) and 23.6 kNm with a limit analysis based approach. The external bending moment was 17.9 kNm under a uniform horizontal load distribution and 23.6 kNm under a segmental profile of horizontal load based on the measurements of the accelerometers (see §5.3.1).

For both the specimens, the theoretical estimate of the ultimate strength resulted in good agreement with the experimental bending moment at collapse, provided that dynamic amplification was considered in the calculation of this latter. The predicted failure mode was also observed in the tests, even if masonry (especially the tuff blocks) also crushed in combination with the detachment of the composite overlay.

It should be noted that the simplifying assumptions of the analytical model do not consider buckling induced TRM detachments (the composite on the compressed side is disregarded), damage accumulation (which may largely affect the response of a specimen during a long shake table test session) and the presence of connectors (which significantly contributed to the response of the retrofitted stone wall). Despite these limitations, based on the comparisons made with the results of the present shake table tests, the approach proposed by existing literature appears reliable for the design of seismic retrofitting and for a preliminary assessment of TRM retrofitted walls under dynamic loading.

7 Conclusions

A shake table test was carried out on two full-scale masonry walls, one built in regular tuff blocks and one with rubble stones, which were constrained on top to induce out-of-plane vertical bending under earthquake base motion. The experimental investigation provided information on their dynamic behaviour and on the enhancement of seismic capacity attained by externally bonded reinforcements with mortar-based composites.

As for the unreinforced specimens, failure occurred by the development of a hinge at about 3/4 of the height and the onset of a collapse mechanism with a peak base acceleration of 0.86 g for the tuff wall and 0.53 g for the stone wall. The lower capacity of the stone wall with respect to the tuff one should be attributed to the higher mass density, which entailed higher inertial forces under the same earthquake base excitation. The seismic capacity exhibited by the unreinforced walls appeared higher than that estimated for existing masonry structures in post-earthquake activities. This might be due to the effects of openings, interaction with other structural members including those transferring horizontal thrusts, pre-existing damage/deterioration, which were not reproduced in the tests. Information collected during surveys also indicates that the stone structures in historic centres are often weaker than that built within this study, due to the presence of smaller stones, thicker mortar joints, wider voids, weak inner core, etc.

After a first test session, the walls were retrofitted using either a Steel Reinforced Grout (SRG) system comprising a unidirectional steel textile or a Basalt Textile Reinforced Mortar (BTRM) composite, which makes use of a bidirectional basalt mesh. Both fabrics were bonded with a lime-based mortar.

The SRG, applied to the tuff wall, enhanced the maximum acceleration attained in shake table tests by 138% (2.05 g) and the deflection capacity by 12% (110 mm vs. 98 mm). Despite applied in discrete strips, SRG resulted effective thanks to the high tensile strength of the steel cords and the good adhesion with the substrate.

The BTRM overlay, installed over the entire surface of the stone wall, ensured a similar increase of the strength (113%, 1.13 g), whereas the maximum recorded displacements decreased from 134 to 115 mm (–14%) in this case. The necessity of reinforcing the wall over its entire surface (in order to prevent disaggregation), required the use of a mesh instead of the unidirectional textile, but this also allowed the application of a relatively weaker material (basalt in place of steel). Transversal steel connectors effectively avoided leaf separation and improved the load transfer capacity from the masonry to the reinforcement. Nevertheless, the bond strength of the BTRM overlay and the substrate appears improvable, and this could be achieved, for instance, by a wider grid spacing (keeping the same design thickness). For both the systems, the long term durability still represents an open issue that deserves further research, in view of their use within structural rehabilitation activities. More generally speaking, the possibility of monitoring and controlling externally bonded reinforcements after some years have passed from retrofitting is expected to become a need related to safety and sustainability in the next future.

TRM systems reduced the out-of-plane displacements under the same seismic input. With respect to the unreinforced walls, the displacement profiles of the retrofitted specimens also showed a wider deflection distribution, their response being more similar to a nearly-elastic beam rather than to a two nearly-rigid block mechanism. Dynamic identification analyses revealed that the repair works (repointing of crushed mortar joints, replacing of broken stone units) and the retrofitting with SRG or BTRM composites compensated for the stiffness reduction caused by damage developed during the test sessions on the unreinforced specimens. The fundamental frequency detected at the beginning of the test series on the retrofitted walls was comparable to that of the unreinforced and undamaged walls, indicating that the application of mortar-based composites did not significantly increase the stiffness of the structural members. Additionally, SRG and BTRM overlays entailed a lower progressive damage accumulation under increasing intensity of the seismic inputs, indicating that retrofitted walls are expected to better sustain strong earthquake sequences.

The ultimate flexural strength was estimated using theoretical approaches suggested by available literature and resulted in good agreement with the experimental bending moment at collapse, provided that this latter was calculated considering dynamic amplification effects, that is, taking into account the accelerations recorded along the wall height rather than just at its base. Despite the simplifying assumptions do not allow to predict buckling induced detachment and progressive damage accumulation, based on the results of the present shake table tests, the existing theoretical approaches appear reliable for the design of seismic retrofitting and for a preliminary assessment of TRM retrofitted walls under dynamic loading.

This study indicates that composite materials with inorganic matrices can be effectively used to protect the building stock in earthquake prone areas. Clearly, their effectiveness relies on the proper installation, which also includes the preparation of the substrate, and on the careful control of the curing conditions (temperature, relative humidity) of the mortars in the construction site. The use of lime-based mortars as matrices, which proved

effective even under severe seismic inputs, makes them suitable for applications to architectural heritage. Finally, thanks to their small thickness, they could be installed during the ordinary maintenance works of the façades. Further tests could provide important information on the influence of the interaction between orthogonal walls, of openings and of a roof. Other masonry types (e.g., brickwork, three-leaves walls) and reinforcement materials (e.g., glass, carbon) could be investigated to gain a deeper understanding on the dynamic behaviour and seismic capacity of TRM retrofitted structures.

Acknowledgements This work was carried out within the Research Projects “Composites with inorganic matrix for sustainable strengthening of architectural heritage” funded by the Italian Ministry for Foreign Affairs (Years 2017–2018, Grant N. PGR00234) and “ReLUIS-DPC 2017, Thematic Area Innovative materials for interventions in seismic areas”, funded by the Italian Department of Civil Protection. S. De Santis, G. de Felice and P. Meriggi acknowledge funding also from the Italian Ministry of Education, University and Research (MIUR), in the frame of the Departments of Excellence Initiative 2018–2022, attributed to the Department of Engineering of Roma Tre University. The shake table test was performed within the Project “CO.B.RA” funded by Lazio Region. Kerakoll SpA (Sassuolo, Italy) is kindly acknowledged for cofunding the research and for providing reinforcement materials.

Compliance with ethical standards

Conflict of interest The authors declare that they have no conflict of interest.

References

- Alecci V, Focacci F, Rovero L, Stipo G, De Stefano M (2016) Extrados strengthening of brick masonry arches with PBO–FRCM composites: experimental and analytical investigations. *Compos Struct* 149:184–196. <https://doi.org/10.1016/j.compstruct.2016.04.030>
- American Concrete Institute (2013) ACI 549.4R-13. Guide to design and construction of externally bonded Fabric-Reinforced Cementitious Matrix (FRCM) systems for repair and strengthening concrete and masonry structures. Farmington Hills, MI, USA
- Ascione L, de Felice G, De Santis S (2015) A qualification method for externally bonded Fiber Reinforced Cementitious Matrix (FRCM) strengthening systems. *Compos B Eng* 78:497–506. <https://doi.org/10.1016/j.compositesb.2015.03.079>
- Babaeidarabad S, De Caso F, Nanni A (2014a) Out-of-plane behavior of URM walls strengthened with Fabric-Reinforced Cementitious Matrix composite. *J Compos Constr* 18(4):04013057. [https://doi.org/10.1061/\(ASCE\)CC.1943-5614.0000457](https://doi.org/10.1061/(ASCE)CC.1943-5614.0000457)
- Babaeidarabad S, Loreto G, Nanni A (2014b) Flexural strengthening of RC beams with an externally bonded Fabric-Reinforced Cementitious Matrix. *J Compos Constr* 18(5):04014009. [https://doi.org/10.1061/\(ASCE\)CC.1943-5614.0000473](https://doi.org/10.1061/(ASCE)CC.1943-5614.0000473)
- Bellini A, Incerti A, Bovo M, Mazzotti C (2017) Effectiveness of FRCM reinforcement applied to masonry walls subject to axial force and out-of-plane loads evaluated by experimental and numerical studies. *Int J Archit Herit* 12(3):376–394. <https://doi.org/10.1080/15583058.2017.1323246>
- Carozzi FG, Milani G, Poggi C (2014) Mechanical properties and numerical modeling of Fabric Reinforced Cementitious Matrix (FRCM) systems for strengthening of masonry structures. *Compos Struct* 107:711–725. <https://doi.org/10.1016/j.compstruct.2013.08.026>
- CEN, European Committee for Standardization. EN 1996 (2005) Eurocode 6: design of masonry structures
- CEN, European Committee for Standardization. EN 998-2:2016 (2016) Specification for mortar for masonry—part 2: masonry mortar
- Chen SP (2010) Out-of-plane behavior of masonry walls strengthened with ferrocement. *Adv Mater Res* 163–167:3545–3550. <https://doi.org/10.4028/www.scientific.net/AMR.163-167.3545>
- Colajanni P, De Domenico F, Recupero A, Spinella N (2014) Concrete columns confined with fibre reinforced cementitious mortars: experimentation and modelling. *Constr Build Mater* 52:375–384. <https://doi.org/10.1016/j.conbuildmat.2013.11.048>
- CNR, Consiglio Nazionale delle Ricerche. CNR DT 215/2018 (2018) Istruzioni per la Progettazione, l'Esecuzione ed il Controllo di Interventi di Consolidamento Statico mediante l'utilizzo di Compositi Fibrorinforzati a Matrice Inorganica (in Italian)

- Costa AA, Arêde A, Costa A, Oliveira CS (2012) Out-of-plane behaviour of existing stone masonry buildings: experimental evaluation. *Bull Earthq Eng* 10(1):93–111. <https://doi.org/10.1007/s10518-011-9332-9>
- D'Antino T, Carloni C, Sneed LH, Pellegrino C (2014) Matrix-fiber bond behavior in PBO FRCC composites: a fracture mechanics approach. *Eng Fract Mech* 117:94–111. <https://doi.org/10.1016/j.engfracmec.2014.01.011>
- D'Ayala DF, Paganoni S (2011) Assessment and analysis of damage in L'Aquila historic city centre after 6th April 2009. *Bull Earthq Eng* 9(1):81–104. <https://doi.org/10.1007/s10518-010-9224-4>
- Dalalbashi A, Ghiassi B, Oliveira DV, Freitas A (2018) Fiber-to-mortar bond behavior in TRM composites: effect of embedded length and fiber configuration. *Compos B Eng* 152:43–57. <https://doi.org/10.1016/j.compositesb.2018.06.014>
- D'Antino T, Carozzi FG, Colombi P, Poggi C (2018) Out-of-plane maximum resisting bending moment of masonry walls strengthened with FRCC composites. *Compos Struct* 202:881–896. <https://doi.org/10.1016/j.compstruct.2018.04.054>
- De Canio G, de Felice G, De Santis S, Giocoli A, Mongelli M, Paolacci F, Roselli I (2016) Passive 3D motion optical data in shaking table tests of a SRG-reinforced masonry wall. *Earthq Struct* 10(1):53–71. <https://doi.org/10.12989/eas.2016.10.1.053>
- de Felice G, De Santis S, Garmendia L, Ghiassi B, Larrinaga P, Lourenço PB, Oliveira DV, Paolacci F, Papanicolaou CG (2014) Mortar-based systems for externally bonded strengthening of masonry. *Mater Struct* 47(12):2021–2037. <https://doi.org/10.1617/s11527-014-0360-1>
- de Felice G, De Santis S, Lourenço PB, Mendes N (2017) Methods and challenges for the seismic assessment of historic masonry structures. *Int J Archit Herit* 11(1):143–160. <https://doi.org/10.1080/15583058.2016.1238976>
- de Felice G, Aiello MA, Caggegi C, Ceroni F, De Santis S, Garbin E, Gattesco N, Hojdyš L, Krajewski P, Kwiecień A, Leone M, Lignola GP, Mazzotti C, Oliveira D, Papanicolaou CG, Poggi C, Triantafyllou T, Valluzzi MR, Viskovic V (2018) Recommendation of RILEM Technical Committee 250-CSM: test method to characterize the Textile Reinforced Mortar to substrate bond behaviour. *Mater Struct* 51(4):95. <https://doi.org/10.1617/s11527-018-1216-x>
- De Santis S (2017) Bond behaviour of Steel Reinforced Grout for the extrados strengthening of masonry vaults. *Constr Build Mater* 150:367–382. <https://doi.org/10.1016/j.conbuildmat.2017.06.010>
- De Santis S, Casadei P, De Canio G, de Felice G, Malena M, Mongelli M, Roselli I (2016a) Seismic performance of masonry walls retrofitted with Steel Reinforced Grout. *Earthq Eng Struct Dyn* 54(2):229–251. <https://doi.org/10.1002/eqe.2625>
- De Santis S, Napoli A, de Felice G, Realfonzo R (2016b) Strengthening of structures with Steel Reinforced Polymers: a state-of-the-art review. *Compos B Eng* 104:87–110. <https://doi.org/10.1016/j.compositesb.2016.08.025>
- De Santis S, Carozzi FG, de Felice G, Poggi C (2017a) Test methods for Textile Reinforced Mortar characterization. *Compos B Eng* 127:121–132. <https://doi.org/10.1016/j.compositesb.2017.03.016>
- De Santis S, Ceroni F, de Felice G, Fagone M, Ghiassi B, Kwiecień A, Lignola GP, Morganti M, Santandrea M, Valluzzi MR, Viskovic A (2017b) Round robin test on tensile and bond behaviour of Steel Reinforced Grout systems. *Compos B Eng* 127:100–120. <https://doi.org/10.1016/j.compositesb.2017.03.052>
- De Santis S, Hadad HA, Caso De, Basalo F, de Felice G, Nanni A (2018a) Acceptance criteria for tensile characterization of Fabric Reinforced Cementitious Matrix (FRCC) systems for concrete and masonry repair. *J Compos Constr* 22(6):04018048. [https://doi.org/10.1061/\(ASCE\)CC.1943-5614.0000886](https://doi.org/10.1061/(ASCE)CC.1943-5614.0000886)
- De Santis S, Roscini F, de Felice G (2018b) Full-scale tests on masonry vaults strengthened with Steel Reinforced Grout. *Compos B Eng* 141:20–36. <https://doi.org/10.1016/j.compositesb.2017.12.023>
- De Santis S, Roscini F, de Felice G (2019) Retrofitting of masonry vaults by basalt-Textile Reinforced Mortar overlays. *Int J Archit Herit*. <https://doi.org/10.1080/15583058.2019.1597947>
- Derakhshan H, Griffith MC, Ingham JM (2013) Airbag testing of multi-leaf unreinforced masonry walls subjected to one-way bending. *Eng Struct* 57:512–522. <https://doi.org/10.1016/j.engstruct.2013.10.006>
- Dizhur D, Dhakal RP, Bothara J, Ingham J (2016) Building typologies and failure modes observed in the 2015 Gorkha (Nepal) earthquake. *Bull NZ Soc Earthq Eng* 49(2):211–232
- Fossetti M, Minafò G (2015) Strengthening of masonry columns with BFRCM or with steel wires: an experimental study. *Fibers* 4(2):15. <https://doi.org/10.3390/fib4020015>
- Garmendia L, Larrinaga P, García D, Marcos I (2014) Textile-Reinforced Mortar as strengthening material for masonry arches. *Int J Archit Herit* 8(5):627–648. <https://doi.org/10.1080/15583058.2012.704480>
- Gattesco N, Boem I (2015) Numerical simulation of the out-of-plane performance of masonry walls strengthened with a GFRP reinforced mortar. In: International conference on civil, structural and environmental engineering computing (CC2015). Civil-Comp Press

- Gattesco N, Boem I (2017) Out-of-plane behavior of reinforced masonry walls: experimental and numerical study. *Compos B Eng* 128:39–52. <https://doi.org/10.1016/j.compositesb.2017.07.006>
- Giaretton M, Valluzzi MR, Mazzon N, Modena C (2017) Out-of-plane shake-table tests of strengthened multi-leaf stone masonry walls. *Bull Earthq Eng* 15(10):4299–4317. <https://doi.org/10.1007/s10518-017-0125-7>
- Gonzalez-Libreros JH, Sneed LH, D'Antino T, Pellegrino C (2017) Behavior of RC beams strengthened in shear with FRP and FRCM composites. *Eng Struct* 150:830–842. <https://doi.org/10.1016/j.engstruct.2017.07.084>
- Graziotti F, Tomassetti U, Penna A, Magenes G (2016) Out-of-plane shaking table tests on URM single leaf and cavity walls. *Eng Struct* 125:455–470. <https://doi.org/10.1016/j.engstruct.2016.07.011>
- Hamed E, Rabinovitch O (2010) Failure characteristics of FRP-strengthened masonry walls under out-of-plane loads. *Eng Struct* 32(8):2134–2214. <https://doi.org/10.1016/j.engstruct.2010.03.016>
- ICC-ES (2016) AC434. Acceptance criteria for masonry and concrete strengthening using Fabric-Reinforced Cementitious Matrix (FRCM) and Steel Reinforced Grout (SRG) composite system. Whittier, CA
- Kariou FA, Triantafyllou SP, Bournas DA, Koutas LN (2018) Out-of-plane response of masonry walls strengthened using textile-mortar system. *Constr Build Mater* 165:769–781. <https://doi.org/10.1016/j.conbuildmat.2018.01.026>
- Lignola GP, Caggegi C, Ceroni F, De Santis S, Krajewski P, Lourenço PB, Morganti M, Papanicolaou C, Pellegrino C, Prota A, Zuccarino L (2017) Performance assessment of basalt FRCM for retrofit applications on masonry. *Compos B Eng* 128:1–18. <https://doi.org/10.1016/j.compositesb.2017.05.003>
- Lourenço PB, Mendes N, Ramos LF, Oliveira DV (2011) Analysis of masonry structures without box behaviour. *Int J Archit Herit* 5(4–5):369–382. <https://doi.org/10.1080/15583058.2010.528824>
- Lourenço PB, Avila L, Vasconcelos G, Alves JP, Mendes N, Costa AC (2013) Experimental investigation on the seismic performance of masonry buildings using shaking table testing. *Bull Earthq Eng* 11(4):1157–1190. <https://doi.org/10.1007/s10518-012-9410-7>
- Maia N, Silva J (1998) Theoretical and experimental modal analysis. Research Studies Press, Baldock
- Marcari G, Basili M, Vestroni F (2017) Experimental investigation of tuff masonry panels reinforced with surface bonded basalt Textile-Reinforced Mortar. *Compos B Eng* 108:131–142. <https://doi.org/10.1016/j.compositesb.2016.09.094>
- Mendes N, Lourenço PB, Campos-Costa A (2014) Shaking table testing of an existing masonry building: assessment and improvement of the seismic performance. *Earthq Eng Struct Dyn* 43:247–266. <https://doi.org/10.1002/eqe.2342>
- Meriggi P, de Felice G, De Santis S (2019) Design of the out-of-plane strengthening of masonry walls with Fabric Reinforced Cementitious Matrix composites. **(under review)**
- Mongelli M, Roselli I, De Canio G, Ambrosino F (2018) Quasi real-time FEM calibration by 3D displacement measurements of large shaking table tests using HPC resources. *Adv Eng Softw* 120:14–25. <https://doi.org/10.1016/j.advengsoft.2016.07.005>
- Napoli A, Realfonzo R (2015) Reinforced concrete beams strengthened with SRP/SRG systems: experimental investigation. *Constr Build Mater* 93:654–677. <https://doi.org/10.1016/j.conbuildmat.2015.06.027>
- Papanicolaou CG, Triantafyllou TC, Papatthasiou M, Karlos K (2008) Textile reinforced mortar (TRM) versus FRP as strengthening material of URM walls: out-of-plane cyclic loading. *Mater Struct* 41(1):143–157. <https://doi.org/10.1617/s11527-007-9226-0>
- Papanicolaou CG, Triantafyllou TC, Lekka M (2011) Externally bonded grids as strengthening and seismic retrofitting materials of masonry panels. *Constr Build Mater* 25(2):504–515. <https://doi.org/10.1016/j.conbuildmat.2010.07.018>
- Razavizadeh A, Ghiassi B, Oliveira DV (2014) Bond behavior of SRG-strengthened masonry units: testing and numerical modeling. *Constr Build Mater* 64:387–397. <https://doi.org/10.1016/j.conbuildmat.2014.04.070>
- Sorrentino L, D'Ayala D, de Felice G, Griffith M, Lagomarsino S, Magenes G (2017) Review of out-of-plane seismic assessment techniques applied to existing masonry buildings. *Int J Archit Herit* 11(1):2–21. <https://doi.org/10.1080/15583058.2016.1237586>
- Sorrentino L, Cattari S, Da Porto F (2018) Seismic behaviour of ordinary masonry buildings during the 2016 central Italy earthquakes. *Bull Earthq Eng*. <https://doi.org/10.1007/s10518-018-0370-4>
- Tondelli M, Beyer K, DeJong M (2016) Influence of boundary conditions on the out-of-plane response of brick masonry walls in buildings with RC slabs. *Earthq Eng Struct Dyn* 45(8):1337–1356. <https://doi.org/10.1002/eqe.2710>
- Vaculik J, Griffith MC (2018) Out-of-plane shaketable testing of unreinforced masonry walls in two-way bending. *Bull Earthq Eng* 16(7):2839–2876. <https://doi.org/10.1007/s10518-017-0282-8>

- Valluzzi MR, Da Porto F, Garbin E, Panizza M (2014) Out-of-plane behavior of infill masonry panels strengthened with composite materials. *Mater Struct* 47(12):2131–2145. <https://doi.org/10.1617/s11527-014-0384-6>
- Velazquez-Dimas JI, Ehsani MR, Saadatmanesh H (2000) Out-of-plane behaviour of brick masonry walls strengthened with fiber composites. *ACI Struct J* 97(3):377–387

Publisher's Note Springer Nature remains neutral with regard to jurisdictional claims in published maps and institutional affiliations.